Institute of Physics

Master's Thesis

Growth and characterization of colloidal supercrystals formed by PbTe/PbS core-shell nanocrystals

Maria Reitgruber, BSc.

September 2022

MONTANUNIVERSITÄT LEOBEN
www.unileoben.ac.at

EIDESSTATTLICHE ERKLÄRUNG

Ich erkläre an Eides statt, dass ich diese Arbeit selbständig verfasst, andere als die angegebenen Quellen und Hilfsmittel nicht benutzt, und mich auch sonst keiner unerlaubten Hilfsmittel bedient habe.

Ich erkläre, dass ich die Richtlinien des Senats der Montanuniversität Leoben zu "Gute wissenschaftliche Praxis" gelesen, verstanden und befolgt habe.

Weiters erkläre ich, dass die elektronische und gedruckte Version der eingereichten wissenschaftlichen Abschlussarbeit formal und inhaltlich identisch sind.

Datum 07.09.2022

_____
Unterschrift Verfasser/in
Maria Reitgruber

Acknowledgements

First, I want to thank my supervisor Rainer T. Lechner for allowing me to explore such an interesting field of research and for assisting me with advice and support whenever I needed it. It has always been a pleasure for me to discuss my scientific results with such a creative mind as his. I also want to thank Maria Ibáñez and her research group from the Institute of Science and Technology Austria for providing the samples for this thesis.

Next, I want to thank Oskar Paris for his helpful input throughout my work. As the head of the institute, he made it possible for me to write this thesis, as well as to gain a lot of experience during working as a student assistant. Additionally, I want to thank Gerhard Popovsky for his support and for developing multiple softwares for visualizing and editing SAXS data. Not much explanation was needed to use them, but Gerhard and Rainer were always ready to help.

I want to thank all my colleagues at the Institute of Physics for their constant support and for creating a friendly and warm working environment. Between the writing sessions, I was always looking forward to the joyful coffee breaks with Malina Jop, Taha Honaramooz, Sebastian Stock, Max Rauscher, and Nadine Aichberger. And in times of desperation over data evaluation, Markus Kratzer always managed to put a smile on my face with his jokes.

Finally, I want to thank my family for their support and guidance not only during my study times but through all the stages of my life. Without their help, I probably would not be where I am right now. I also want to thank my friends for accompanying me through good, as well as difficult times, and for their helpful advice.

Abstract

To obtain functional nanomaterials and integrate them into technical devices, nanocrystals (NCs) must be aligned into ordered superstructures, similar to the arrangement of atoms in a crystalline solid material. Thereby, the electronic properties of the single NCs are enhanced, so they can further be applied in devices such as heat sensors and solar cells. To what extent these properties can be magnified depends on the positional and orientational order of the NCs within the supercrystal.

In this work, the self-assembly of semiconducting core-shell PbTe/PbS NCs to supercrystals was investigated. These particles are thermoelectric, and their ability to convert heat to electricity makes them an important candidate e.g. for waste heat recovery and active cooling [1]. The NCs were provided by M. Ibáñez at the Institute of Science and Technology in Austria (ISTA), dispersed in a solvent. The crystal structure of the particles was determined using X-ray diffraction (XRD). Then, self-assembly through two mechanisms: solvent evaporation and diffusion of a non-solvent into a solvent were investigated *in-situ*, as well as *ex-situ*, using small-angle X-ray scattering (SAXS). The resulting superstructures were later observed under the optical microscope and compared to the results from the SAXS measurements. Then, the impact of the NCs' shape on the superstructure was investigated to recreate their positional and orientational order within the supercrystals.

The main resulting structure during both mechanisms was determined to be body-centered cubic (bcc). During evaporation of the solvent a much denser, but less ordered structure, than during diffusion, was obtained. During the diffusion process, hexagonal close-packed (hcp) stacking faults were found in between the bcc lattice at certain positions. The *ex-situ* measurements, which were performed a few weeks later, revealed large supercrystals with a mostly hexagonal structure. Apparently, the supercrystals rearranged themselves during this period. In the microscopy images taken afterwards, large crystals can be seen, which correlate with the results from the SAXS measurements.

In this work it has been shown, that through the diffusion of a non-solvent into the solvent, as well as through evaporation of the solvent, ordered crystalline structures can be built from PbTe/PbS core-shell nanoparticles. This information is essential for further studies of the electronic properties of the supercrystals, as they highly depend on their internal structure.

Kurzfassung

Um funktionelle Nanomaterialien herzustellen und sie in technische Geräte zu integrieren, müssen Nanokristalle (NCs) zu geordneten Superstrukturen angeordnet werden, ähnlich den Atomen in einem kristallinen Feststoff. Dadurch lassen sich die elektronischen Eigenschaften der einzelnen NCs verbessern und sie können in technische Geräte, wie beispielsweise Wärmesensoren und Solarzellen, eingebaut werden. Inwieweit diese Eigenschaften verbessert werden können, hängt von der Lage und Ausrichtung der NCs im Superkristall ab.

In dieser Arbeit wurde die Selbstorganisation von halbleitenden core-shell PbTe/PbS NCs zu Superkristallen untersucht. Diese Teilchen sind thermoelektrisch: ihre Fähigkeit, Wärme in elektrischen Strom umzuwandeln, macht sie zu einem wichtigen Kandidaten für die Rückgewinnung von Abwärme und aktive Kühlung [1]. Die NCs wurden von M. Ibáñez vom Institute of Research and Technology Austria (ISTA) zur Verfügung gestellt, als dispergierte Teilchen in einem Lösungsmittel. Ihre Kristallstruktur wurde mittels Röntgenbeugung (XRD) bestimmt. Anschließend wurde deren Superkristallisation durch zwei Mechanismen, Lösungsmittelverdampfung und Diffusion eines Nichtlösungsmittels in das Lösungsmittel, sowohl *in-situ* als auch *ex-situ* mittels Kleinwinkelröntgenstreuung (SAXS) untersucht. Die dabei entstandenen Superstrukturen wurden unter einem Lichtmikroskop betrachtet und mit den Ergebnissen der SAXS-Messungen verglichen. Anschließend wurde der Einfluss der Form der NCs auf die Superstruktur analysiert, um herauszufinden, wie sie innerhalb der Superkristalle positioniert und orientiert sind.

Die Struktur, die bei beiden Mechanismen am häufigsten entstand, war die kubisch-raumzentrierte Struktur (bcc). Durch Verdampfung des Lösungsmittels ergab sich eine wesentlich dichtere, aber weniger geordnete Struktur als durch Diffusion. Während des Diffusionsprozesses fanden wir an bestimmten Positionen hexagonal dicht gepackte (hcp) Stapelfehler im bcc-Gitter. Die *Ex-situ*-Messungen, die einige Wochen später durchgeführt wurden, offenbarten große Superkristalle mit überwiegend hexagonaler Struktur. Offensichtlich haben sich die Superkristalle in dieser Zeit neu angeordnet. In den anschließend im Lichtmikroskop aufgenommenen Bildern sind große Kristalle zu sehen, die mit den Ergebnissen der SAXS-Messungen korrelieren.

In dieser Arbeit wurde gezeigt, dass sowie durch Diffusion eines Nicht-Lösungsmittels in ein Lösungsmittel, als auch durch das Verdampfen des Lösungsmittels geordnete kristalline

Strukturen aus PbTe/PbS-core-shell NCs gebildet werden können. Diese Information ist für weiterführende Untersuchungen der elektronischen Eigenschaften der Superkristalle essenziell, da diese in hohem Maße von deren inneren Strukturen abhängig sind.

Abbreviations

PbTe	lead telluride
PbS	lead sulphide
NC	nanocrystal
ZT	figure of merit
OA	oleic acid
bcc	body-centred cubic
fcc	face-centred cubic
hcp	hexagonal close-packed
PD	packing density
m	multiplicity factor
a, b	lattice constant
c	c-axis
XRD	X-ray diffraction
SAXS	small-angle X-ray scattering
WAXS	wide-angle X-ray scattering
FWHM	full width half maximum
q/Q	scattering vector
φ	azimuthal angle
σ	standard deviation
SC	supercrystal
D	particle diameter
D_{soft}	particle diameter, including effective ligand length
ID	interparticle distance
L	ligand length
IF	interface

Content

1. Introduction

The spontaneous organization of basic building blocks, such as atoms and molecules, into larger and more complex structures, is among the most studied phenomena in science and a fundamental principle of how nature fabricates functional materials. Crystals not only are beautiful, admirable objects, but they also possess significant physical properties, which highly depend on their structure and shape. In its classical form, crystallization is described as a layer-wise deposition of atoms or molecules on the surface of a crystal nucleus, amplifying it within the limits set by the crystal unit cell. Nevertheless, this classical model does not apply for many real crystallization processes, like the natural self-assembly of nanometre-sized particles in several biomaterials (Figure 1) [2].
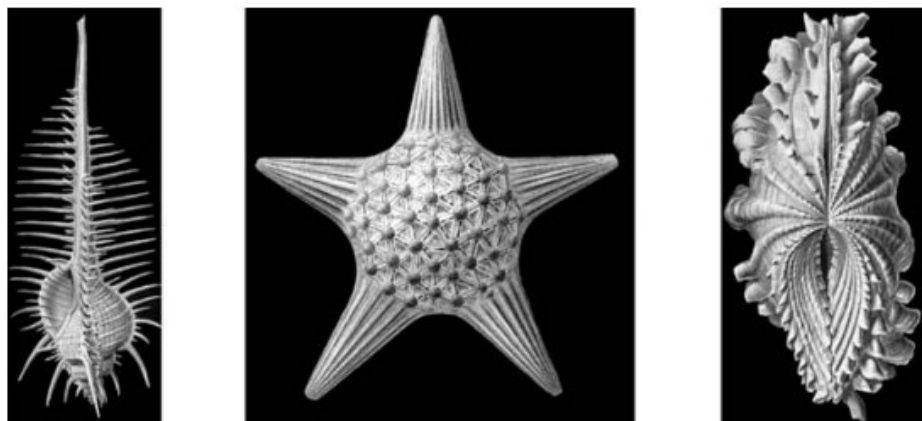

Figure 1: Various Biomaterials with complex forms. Left: Prosobranchia, centre: Thalamophora, right: Acephala. Used with permission from Ref. [2]; permission conveyed through Copyright Clearance Center, Inc.

By fabricating artificial colloidal nanocrystals (NCs) and studying their behaviour, scientists are trying to mimic these natural processes, to finally design functional materials with peculiar properties [3]. Thermoelectric core-shell PbTe/PbS NCs represent such successfully synthesised nanoparticles. Their ability to generate electrical power from heat has drawn growing research interest especially nowadays, when the demand for clean energy and non-renewable fossil fuels has never been larger. For instance, thermoelectric generators harvesting electricity from waste heat represent a promising way to generate alternative energy [4]. Despite the high potential, thermoelectrics are banned from multiple markets due to their relatively low efficiencies. Until today, nearly all highly efficient thermoelectrics are nanostructured [3]. An ordered alignment of these NCs is crucial, as properties like charge transport do not only depend on the particle itself, but also on the structure and directions of the superlattice [5].

This thesis aims to investigate the growth process of large, highly ordered supercrystals from thermoelectric PbTe/PbS core-shell nanoparticles. We want to discover the inner structures of the governed supercrystals and correlate them with the external growth conditions. These fundamental investigations build the foundation of further studies on the physical properties of the governed structures, as well as on finding optimal ways to build nanostructured devices in large-scale processes.

As previously mentioned, thermoelectric PbTe/PbS core-shell NCs were investigated in this thesis. PbTe and PbS are both semiconductors, and their combination into a core-shell structure affects an enhancement of electrical properties, compared to their bulk counterparts. The NCs were synthesized at the Institute of Science and Technology in Austria (ISTA) and provided in a form of colloidal particles dispersed in a solvent. The self-assembly of those particles through evaporation of the solvent and diffusion of the NC-solvent mixture into a non-solvent was studied. The growth and structures of the superlattices were observed *in-situ* and *ex-situ* using X-rays, specifically the X-ray diffraction (XRD) and small-angle X-ray scattering (SAXS) methods. The resulting structures have later been observed under the optical microscope.

2. Fundamentals

1.1.   Structure and properties of PbTe/PbS nanoparticles

The semiconducting properties of lead chalcogenides, compounds of lead with sulphur, selenium, or tellurium, have been investigated for many years: the high thermoelectric power of PbS was discovered by Seebeck back in 1822 [4,6].

The performance of a thermoelectric is measured by its figure of merit:

$$ZT = \frac{\sigma S^2 T}{\kappa} \qquad (1)$$

With the Seebeck coefficient S, the electrical conductivity σ, the thermal conductivity κ and the temperature T [7]. The Seebeck coefficient represents the magnitude of an induced voltage in response to a temperature difference. Only if the average ZT exceeds ~ 3.0, the material could practically be used for energy transfer [1]. Record thermoelectric figures of merit of ~ 1.1 were obtained by M. Ibáñez from PbTe and PbS phases at 710 K, which are about 10 times higher than the pure PbTe and PbS (Figure 2). The highest value ever reported for lead chalcogenides was ~ 2.3, in a 3% Na-doped $(PbTe)_{0.8}(PbS)_{0.2}$ [3].
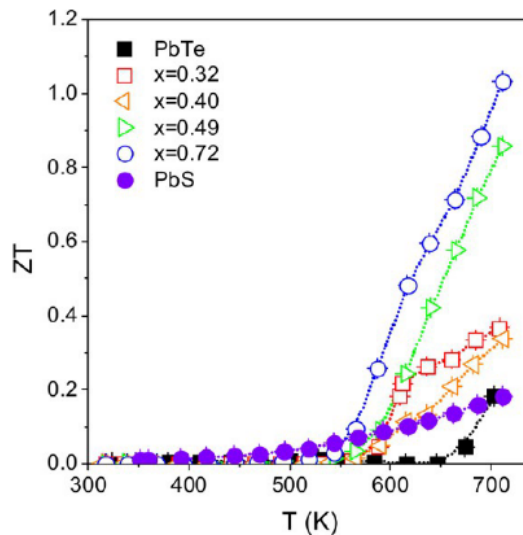

Figure 2: Thermoelectric figure of merit (ZT) of $(PbTe)_{1-x}(PbS)_x$ nanomaterials, compared to their bulk counterparts. Reprinted with permission from Ref. [3]. Copyright 2013 American Chemical Society.

Both PbS and PbTe have the face-centred cubic rock-salt structure with a lattice mismatch of only 0.5 Å (Figure 3 a). Their nature of chemical bonding is usually ionic-covalent, and their carrier mobility is highly temperature dependent [8].

The investigated nanoparticles are built of a PbTe core surrounded by a passivating PbS shell and surface-bound organic molecules, so-called ligands (Figure 3 b). Not only does the shell enhance the stability against oxidation, but it also drastically increases its carrier mobility, as it acts as a strong electron dopant. It has been shown that both PbTe and PbS NCs support ambipolar charge carrier transport, which means that both holes and electrons can be transported from one NC to another. Shelling a PbTe core with a PbS shell makes them exclusively electron-transporting. Due to the wider band gap of the shell, charges are localized within the PbTe-core region (Figure 5). The capability of electron transport with complete suppression of hole transport in the narrow bandgap of the NCs enables its utilization in energy harvesting devices such as thermoelectrics and photovoltaics, where electron transport is vital [9,10]. Shelling NCs can significantly enhance luminescence efficiency for various optical applications like LED and displays [11,8,4].
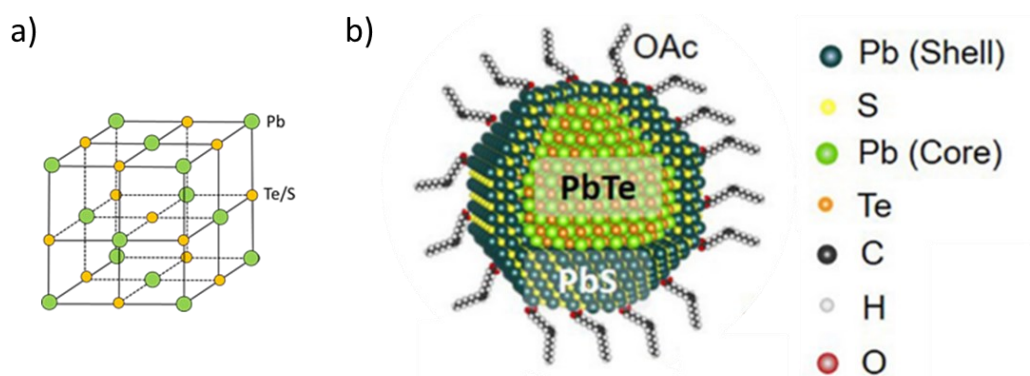

Figure 3: a) Crystal structure of PbTe and PbS and b) schematic illustration of a PbTe /PbS core-shell NC. Used with permission from Ref. [10]; permission conveyed through Copyright Clearance Center, Inc.

The core-shell NCs are usually synthesised in a solution containing ligands, which bind to the surface of the particles. The major role of the ligands is to grant the stability of the nanoparticle dispersion in the solvent they are immersed in. They prevent the NCs from agglomeration during storage and handling and passivate the particle surface [11]. It has been shown that quantum yields, the ratio of photons emitted to photons absorbed, can be increased by covering of the surface with ligands [12]. However, the ligands also act as a barrier for charge transport, and therefore must be removed for device applications [11]. They typically consist of an anchoring group, bound to the NC surface, and a hydrocarbon group tail facing away from it

[13]. In this work, oleic acid (OA) ligands were used to stabilize the NCs in the solvent hexane (Figure 4) [14]. In this non-polar liquid, the OA molecule chains repel one another, thus stabilizing the NC dispersion.
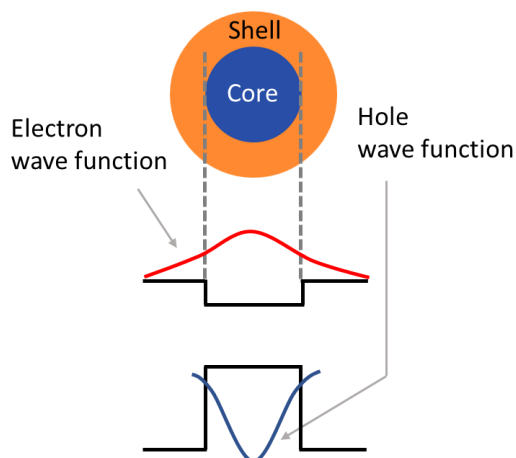

Figure 4: Schematic representation of the energy band diagrams of a core-shell NC.

1.2.   Self-assembly

Self-assembly can be defined as an event occurring spontaneously near a local equilibrium state, that leads to the formation of ordered structures. It is a fundamental principle of how functional materials are built in nature. The formation of DNA, proteins, opals, and nanocrystal superlattices are examples of self-assembly processes [15].

In contrast to molecular building blocks, where binding is regulated by highly specific, strong directional forces, colloidal building blocks are characterized by weak potentials, like the Van der Waals force or hydrogen bonding. There are no long-range attractive interactions in colloidal crystals, but sheer entropy gain by optimization of packing [16].
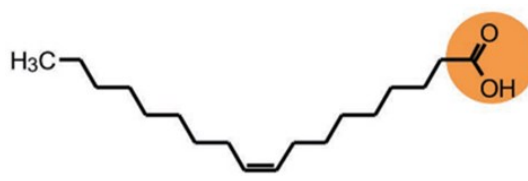

Figure 5: Structural formula of an oleic acid molecule. Used with permission from Ref. [14]; permission conveyed through Copyright Clearance Center, Inc.

For an assembly into an ordered structure, rather than a random assembly, a long-range interaction with a suitable magnitude must be dominant. The magnitude of the particle-particle interaction highly depends on the particle size, whereas its range is within the atomic scale [17].

Dominant driving forces in NC interactions include the NC shape, interactions between ligands, Van der Waals and dipole-dipole interactions between the cores of the nanoparticles, interactions with a substrate or interface, and solvent quality. Typically, for NC with sizes of a few nanometres, van der Waals forces between ligands are much stronger than core-core interactions [18]. In NCs which are not perfectly spherical, the anisotropic profiles and crystal planes may induce dipole moments. The additional facet-selective binding energies of ligands can reinforce this polar interaction.

Highly ordered superstructures can be achieved through solvent evaporation-induced self-assembly on hard substrates or through the diffusion of a non-solvent into the solvent that contains the NCs [19]. For sterically stabilized particles, such as NCs coated with a layer of OA molecules, a good solvent implies a negative free energy of chain-solvent mixing. This causes the hydrocarbon chains to repel one another, thus stabilizing the NC dispersion. When immersed in a non-solvent with a positive chain-solvent mixing energy, the desire to minimize contact with the surrounding liquid induces the contraction of ligand chains and the aggregation of dispersed NCs (Figure 6). Under this condition, the self-assembly of nanoparticles and supercrystal formation is possible. Typical good solvents for hydrocarbon-capped NCs are nonpolar liquids, for example hexane or toluene, whereas the polar ethanol or acetone represent non-solvents [13].
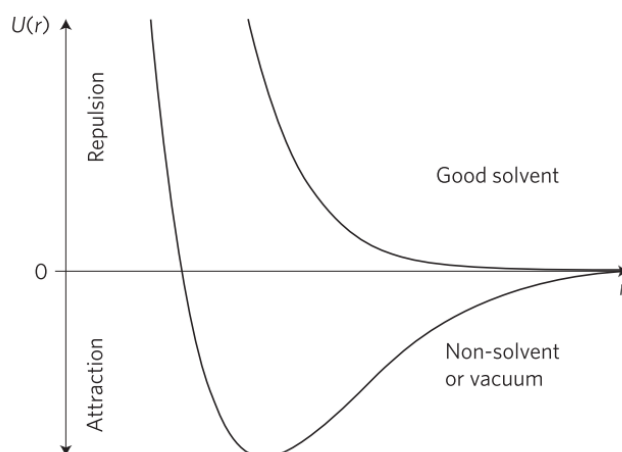

Figure 6: The interaction potential U with the particle distance r for NCs in a good solvent and a non-solvent. Used with permission from Ref. [13]; permission conveyed through Copyright Clearance Center, Inc.

1.3. Crystallography

Humans deal with symmetry constantly throughout the day, starting from a glance in the mirror and ending by falling into a bed with balanced proportions. But what many might not be aware of, is the high importance of the concept of symmetry in science. Ordered atomic structures can be found in various materials including metals, sand and even snow. The physical properties of such solids directly depend on the arrangement of atoms they are built from. Therefore, a comprehensive and formal description of symmetry is necessary [20].

Crystallography describes the arrangement of atoms in crystalline solids. An interatomic potential, which consists of two terms representing short-distance repulsion and long-distance attraction between particles, is responsible for this periodic ordering (Figure 7). Usually, the shape of the orbitals and the bonding type determine the crystalline lattice type [21].
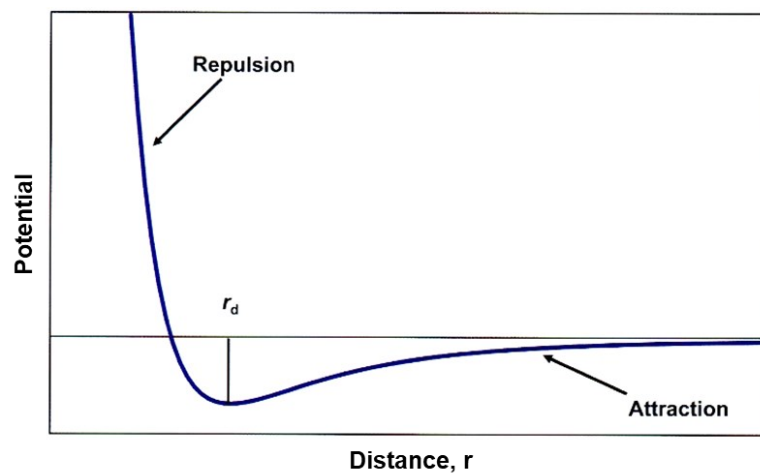

Figure 7: Interatomic potential as a function of interatomic distance r for two neighbouring atoms. The sharp slope on the left side from the equilibrium point r_d is caused by repulsive forces between ions, while attractive forces result in the function approaching zero potential at large distances. Adapted from Ref. [21]; permission conveyed through Copyright Clearance Center, Inc.

In general, crystallization starts from dissolved atoms or ions. The thermodynamic driving force for crystallization is the supersaturation of the solution. It is generated by reducing the solubility of the product in solution. Supersaturated solutions can be prepared by, for instance, a temperature or a pressure jump, or by adding a non-solvent. To be able to grow in solution under supersaturation conditions, crystals need a nucleus to grow from. Surfaces of dispersed components, such as dust particles or crystal seeds, may provide such a starting point of crystallization [2].

E. Zolotoyabko [21] gives the following definition of a crystal: "A crystal can be defined as a 3D object densely built of repeating structural units located at fixed distances from their neighbours, the distances being unchanged across the crystal volume." Therefore, crystals can be described by a lattice, a regular structure, made of many periodic units, called unit cells. Unit cells are the smallest representatives of a crystal and include all components that can be found repeating all over the lattice. Due to limited symmetry options, only a limited number of possible crystals exists in nature. The typical crystal structures for most metallic elements are presented in Figure 8.
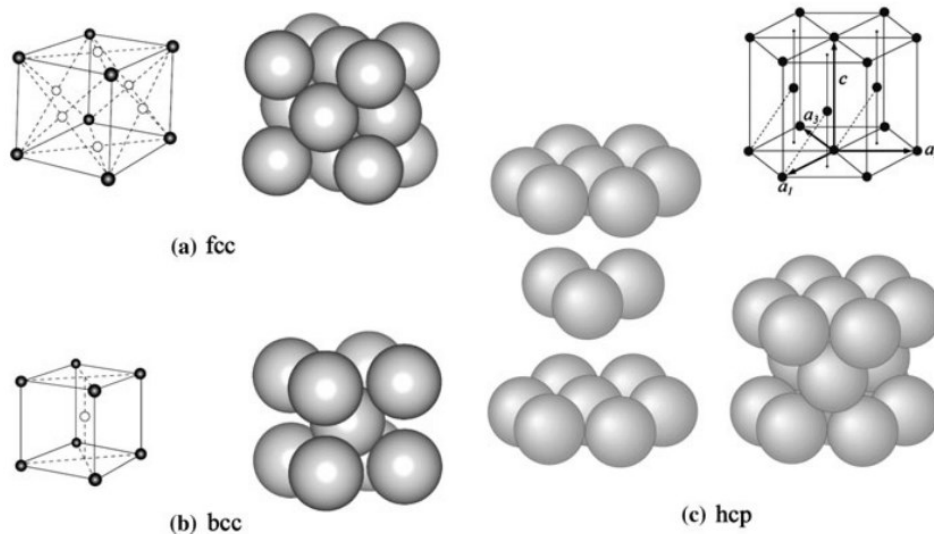

Figure 8: Typical crystal structures of metallic elements, (a) being face-centred cubic (fcc), (b) body-centred cubic (bcc) and (c) hexagonal close packed (hcp). Reproduced with permission from Ref. [22]; permission conveyed through Copyright Clearance Center, Inc.

To illustrate the phenomenon of diffraction from ideal crystal lattices, the concept of the crystallographic plane is introduced. A family of crystallographic planes in a lattice is defined as a set of planes that are parallel to each other and equally spaced. To fully describe planes and directions, the so-called Miller indices, h, k, and l, are employed. They are defined as the reciprocals of the fractional intercepts the plane makes with the crystallographic axes. A plane is commonly described by (hkl), which means that it makes fractional intercepts of $1/h$, $1/k$, $1/l$ with the axes a, b, c (Figure 9 a). Crystallographic directions are described using lines that pass through the origin of the lattice in the direction of interest. Commonly, a notation of [hkl] is used in this case (Figure 9 b). In the hexagonal lattice, a slightly different plane indexing is introduced. The so-called Miller-Bravis indices refer to plane indices with four axes such as (h k i l), instead of Miller Indices (Figure 9 c). The relation of

$$i = -(h + k) \qquad (2)$$

is always satisfied [22].

The value of the spacing between equivalent planes in a crystal lattice is called d-spacing and it can be described as a function of the plane indices and lattice parameters, as shown in Table 1. The packing density PD of a lattice type is defined by the ratio between the volume of atoms in a unit cell and the volume of the unit cell.
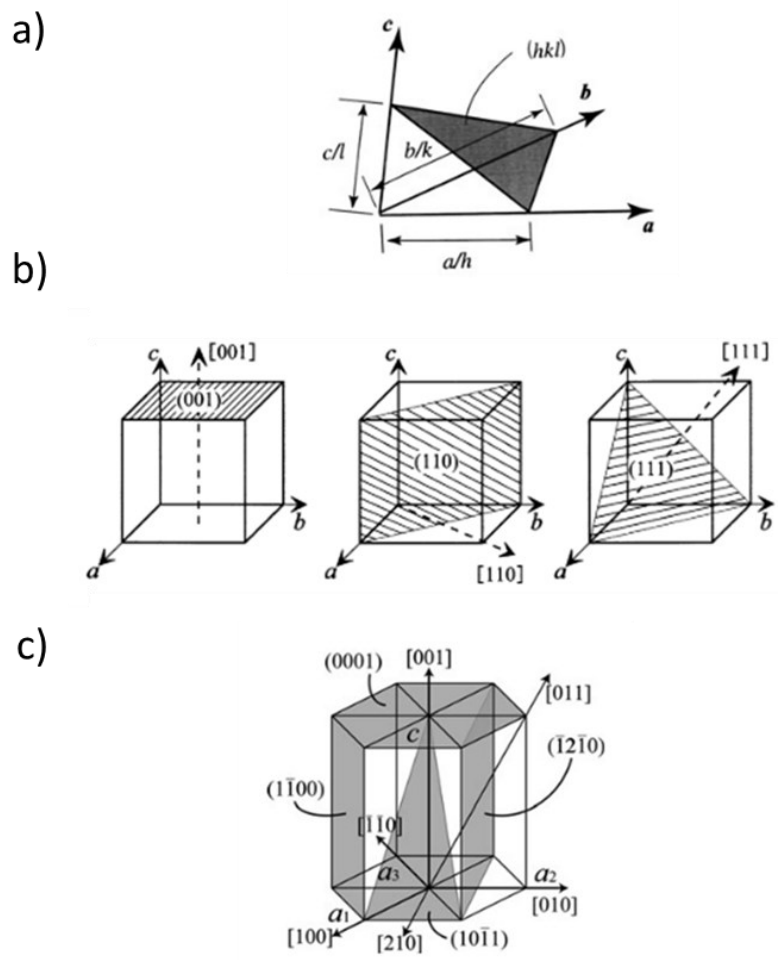

Figure 9: a) Miller indices and b) examples of crystallographic planes and directions for the cubic system and c) for the hexagonal system. Reproduced with permission from Ref. [22]; permission conveyed through Copyright Clearance Center, Inc.

Table 1: Characteristic parameters for the three main crystal lattices [20,22].

Crystal structure	Axial lengths and angles	PD	d-spacing as a function of the lattice constant a	Particle diameter
bcc	$a = b = c$ $\alpha = \beta = \gamma = 90°$	0.68	$\dfrac{1}{d^2} = \dfrac{h^2 + k^2 + l^2}{a^2}$	$D = \dfrac{a \cdot \sqrt{3}}{2}$
fcc	$a = b = c$ $\alpha = \beta = \gamma = 90°$	0.74	$\dfrac{1}{d^2} = \dfrac{h^2 + k^2 + l^2}{a^2}$	$D = \dfrac{a \cdot \sqrt{2}}{2}$
hcp	$a = b \neq c$ $\alpha = \beta = 90°,$ $\gamma = 120°$	0.74	$\dfrac{1}{d^2} = \dfrac{4}{3}\left(\dfrac{h^2+hk+k^2}{a^2}\right) + \dfrac{l^2}{c^2};$ $c = 1.633 \cdot a$	$D = a$

2.4.   Characterization of materials using X-rays

Without a doubt, crystals such as diamonds, emeralds, and rubies, have been enjoyed for centuries for their perfect shapes and astonishing colours. But far less interest has been shown in their internal structure, which explains their shapes and defines their properties, but remains hidden from the naked eye. The inner structure of a crystal can be observed through an infinite number of diffraction patterns it forms upon interaction with electromagnetic waves, for example X-rays [20].

X-rays have a wavelength ranging from $10 - 10^{-3}$ nm, which is much shorter than the wavelength of visible light. They are produced when an electrically charged particle rapidly decelerates. Its kinetic energy is then turned into an electromagnetic wave with the energy of an X-ray. Entering a sample, they are scattered by the electrons in the sample and therefore a reduction of the intensity is detected. If X-rays with the intensity I_0 penetrate a substance, the intensity I after transmission through distance x is given by:

$$I = I_0 e^{-\mu x} \tag{3}$$

The proportional factor μ is called the linear absorption coefficient. The specific values of absorption coefficients for certain X-ray energies and materials are usually tabulated [23]. But only a fraction of the X-ray that hits the material will pass through the sample. Another fraction

will be absorbed and transformed into other forms of energy and a fraction will be scattered in various directions of propagation.

One can define two main scattering processes that occur at the interaction of an X-ray beam with an atom: Tightly bound electrons are set into oscillation and radiate X-rays of the same wavelength as that of the incident beam: This process is known as coherent scattering. In the second process, loosely bound electrons scatter a part of the incident beam and slightly increase the wavelength depending on the scattering angle. This is known as incoherent scattering. If the atom is arranged in a regular pattern with other atoms, like in a crystal, the coherently scattered radiation from all the atoms is reinforced in certain directions and cancelled in others, thus producing diffracted beams [24].

If a set of plane waves hits a lattice, each wave is being diffracted under a certain angle. Depending on the difference in path lengths between two waves, they may interfere either constructive or destructive, resulting in a visible diffraction peak or minimum. If an incident X-ray of wavelength (λ) strikes a crystal in which all the atoms are arranged periodically with the distance d', a diffraction beam with sufficient intensity is only detected if a certain condition, known as Bragg's law, is fulfilled (Figure 10):
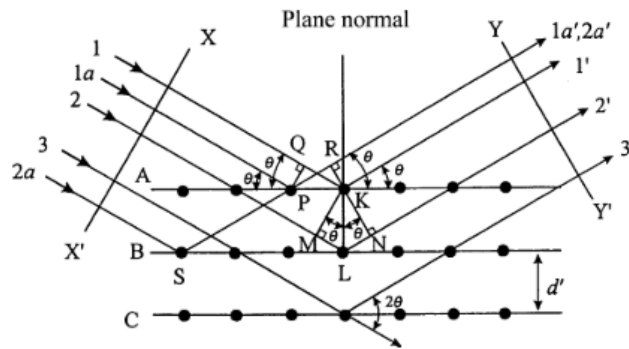
$$2d' \cdot sin\theta = n\lambda \qquad (4)$$

Figure 10: Schematic illustration of Bragg's law, the diffraction of X-rays by a crystal. Reproduced with permission from Ref. [22]; permission conveyed through Copyright Clearance Center, Inc.

For fixed values of both λ and d', the diffraction occurs at several incident angles such as θ_1, θ_2, θ_3 corresponding to $n = 1, 2, 3$. In the first order, the path difference between two neighbouring diffracted X-rays is one wavelength, the path difference between rays 1' and 3' is 2λ, etc. Thus, equation (4) may be rewritten as

$$2d \cdot sin\theta = \lambda \qquad (5)$$

Where $d = d'/n$. This form of Bragg's law is more frequently used [22].

For understanding diffraction and scattering patterns, a more generalized theory than Bragg's law is introduced. Particularly, the concept of the "reciprocal lattice" is highly effective for handling diffraction phenomena of X-rays by a crystal. Here, the usual set of three-dimensional atomic coordinates is called the crystal lattice or real space lattice, while its reverse is called the reciprocal lattice. Sizes and shapes in reciprocal space correlate inversely to the ones in real space (Figure 11).
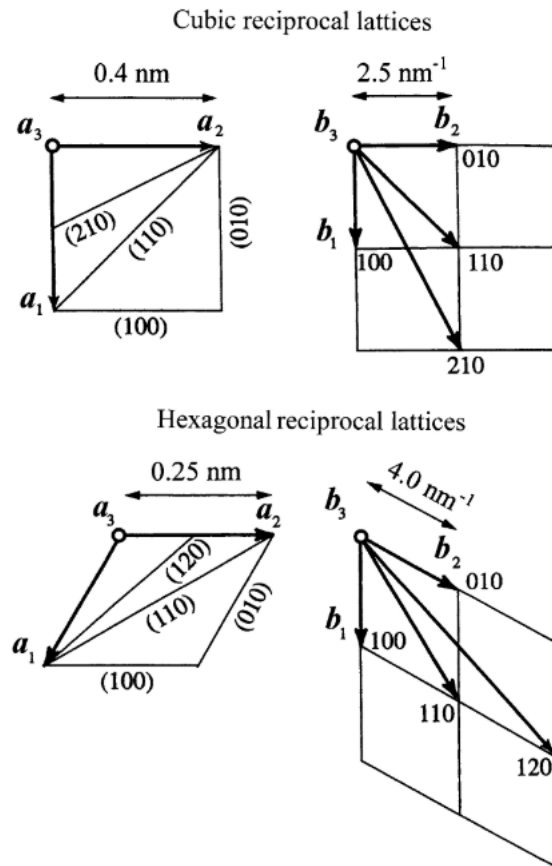

Figure 11: Illustration of crystal lattices (left) and corresponding reciprocal lattices (right) for a cubic system (top) and a hexagonal system (bottom). Adapted from Ref. [22]; permission conveyed through Copyright Clearance Center, Inc.

Regarding the measured intensity from crystals, the information on phase differences between the intensities and the atomic positions in one unit cell are of high importance. The phase difference of X-rays with a path difference of one whole wavelength is 360° (2π in radians). Let us assume that an atom A is placed at (000) and an atom B at the coordinates x, y, z, which can be expressed by the fractional coordinates u, v, w where $u = x/a$, $v = y/b$, $w = z/c$, where a, b and c are the lattice parameters. Under these conditions, the phase difference Φ between the X-rays scattered by atoms A and B is given by

$$\Phi = 2\pi\,(hu + kv + lw) \tag{6}$$

For the (*hkl*) reflection. The variation in electric field intensity E with time t of an electromagnetic wave can be expressed as

$$E = A\exp(2\pi\,i\,\nu\,t) = A\cos(2\pi\,i\,\nu\,t) * iA\cos(2\pi\,\nu\,t) \tag{7}$$

where A is the amplitude and ν is the frequency. The amplitude of the scattered wave from each atom in a unit cell is given by the atomic scattering factor f. It is also called the "form factor" because it depends on the distribution of electrons around the nucleus. When scattering on diluted monodisperse particles is performed, the scattering signal will oscillate in a fashion that is characteristic for the shape of the particle. The form factor is defined as:

$$f = \frac{amplitude\ of\ the\ wave\ scattered\ by\ one\ atom}{amplitude\ of\ the\ wave\ scattered\ by\ one\ electron} \tag{8}$$

By applying certain mathematical relations form complex numbers, we get the following relation for every scattered wave.

$$Ae^{i\Phi} = fe^{2\pi i(hu+kv+lw)} \tag{9}$$

Now, we can sum up the scattered waves from all atoms in a unit cell:

$$F_{hkl} = \sum_{j=1}^{N} f_j e^{2\pi i(hu_j+kv_j+lw_j)} \tag{10}$$

Where N is the number of atoms in the unit cell. F is called the structure factor and represents both the amplitude and the phase of the scattered wave obtained from the summation over all atoms in a unit cell. The intensity of the resultant wave scattered from all atoms in one unit cell in the direction which satisfies Bragg's law is proportional to $|F|^2$. $|F|$ is defined as the ratio:

$$|F| = \frac{amplitude\ of\ the\ wave\ scattered\ by\ all\ the\ atoms\ of\ a\ unit\ cell}{amplitude\ of\ the\ wave\ scattered\ by\ one\ electron} \tag{11}$$

By calculating the structure factor for different lattices and planes, we observe that in some combinations, $|F|^2$ equals to 0. In those cases, the waves cancel each other out being out of phase. The allowed and forbidden reflections for some crystal types are summarized in

Table *2*. The number of equivalent planes in a lattice, which are related by symmetry (for ex. (100), (010), …) is represented by the multiplicity factor (Table 3) [22].

Table 2: Allowed and forbidden reflections for the main metallic crystal lattices.

Crystal type	Allowed reflections
bcc	$h + k + l$ even
fcc	h, k, l all odd or all even
hcp	l even or $\dfrac{h + 2k}{3} \neq n$

Table 3: Allowed reflections for the main metallic crystal lattices and their multiplicity factors.

bcc				fcc				hcp			
h	k	l	m	h	k	l	m	h	k	l	m
1	1	0	12	1	1	1	8	0	0	1	2
2	0	0	6	2	0	0	6	1	0	0	6
2	1	1	24	2	2	0	12	0	0	2	2
2	2	0	12	3	1	1	24	1	0	1	12
3	1	0	24	2	2	2	8	1	0	2	12
2	2	2	8	4	0	0	6	0	0	3	2
3	2	1	48	3	3	1	24	1	1	0	6
4	0	0	6	4	2	0	24	1	1	1	12
4	1	1	36	4	2	2	24	1	0	3	12
4	2	0	24	5	1	1	32	2	0	0	6
3	3	2	24	4	4	0	12	1	1	2	12
4	2	2	24	5	3	1	48	2	0	1	12
4	3	1	48	6	0	0	30	0	0	4	2
5	1	0	24	6	2	0	24	2	0	2	12
5	2	1	48	5	3	3	24	1	0	4	12

2.4.1. Methods

The methods used for characterization of materials with X-rays mostly differ in the angle θ and the distance between detector and sample (Figure 12). The wider the angle, the smaller the structural features that can be measured (Figure 13). Every distance is measured relative to the wavelength of the radiation. To become independent of the wavelength, scattering patterns are usually presented as a function of the scattering vector q which is given by

$$q = \frac{4\pi \, sin\theta}{\lambda} \tag{12}$$

In units of length $^{-1}$.
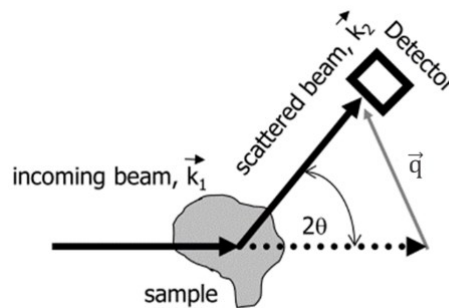
Figure 12: Schematic representation of the detection of an X-ray beam after interaction with a sample [28].

Scattering patterns always represent the reciprocal space [25]. When particles align into ordered structures, the scattering profile can develop a distinct peak. The q-position of its maximum indicates the distance between aligned particles d:
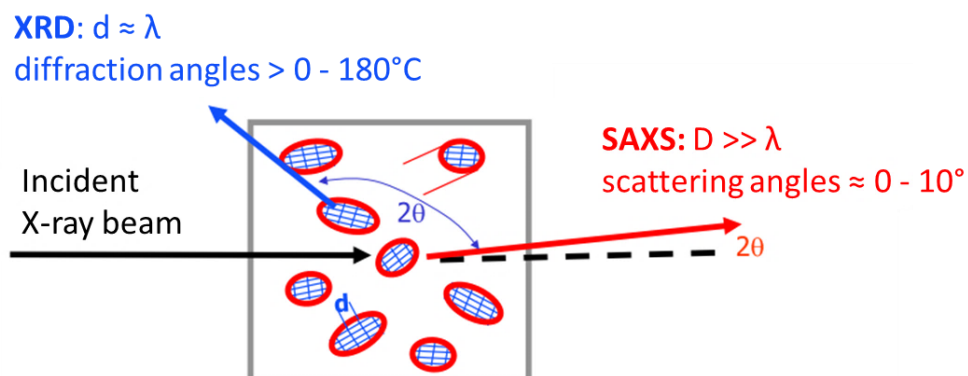
$$q = \frac{2\pi}{d} \tag{13}$$

Figure 13: Illustration of measurement angles and resulting size ranges measured with SAXS and XRD [28].

2.4.1.1.   X-ray diffraction

The method X-ray diffraction (XRD) operates at high angles and can resolute structural features of 10 - 50 nm. For our investigated particles this means that the contained elements and crystal structures can be determined. A diffractometer is an instrument with two axes for independent rotation (Figure 15). This equipment allows obtaining the intensity data of a diffracted X-ray beam as a function of the angle (Figure 14). The 2θ angle typically ranges from 10° to 100°.
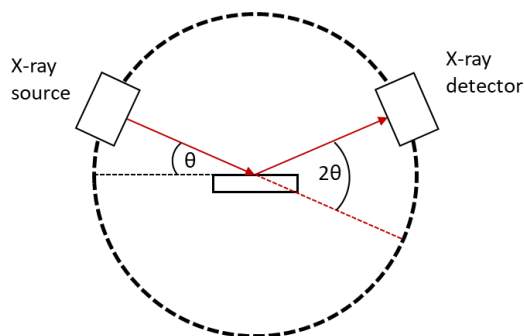
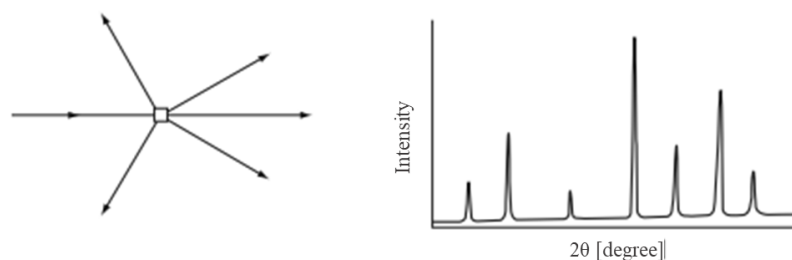Figure 15: Schematic illustration of the XRD experiment.

Figure 14: Scattering by a crystal and the resulting XRD pattern. Peak positions are characteristic for the materials' crystal structure. Reproduced with permission from Ref. [22]; permission conveyed through Copyright Clearance Center, Inc.

2.4.1.2.   X-ray scattering

Small-angle X-ray Scattering (SAXS) is a method to determine the structure of particle systems. As the name indicates, the X-rays are sent through the sample at a low angle of 0.1°-10° ($2\theta = 20°$) (Figure 16). Thus, the particle sizes that can be measured with SAXS range from 1 to about 600 nm. Wide angle X-ray scattering (WAXS) can be performed on the same instrument as SAXS but with a shorter sample-to-detector distance, to be able to cover a wider q-range.
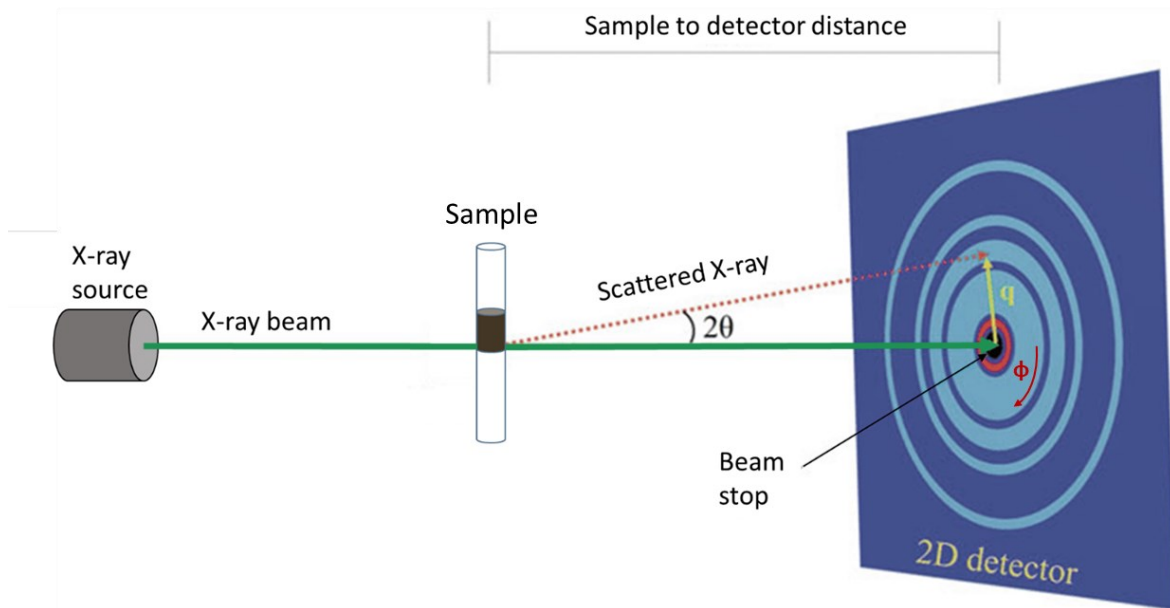
Figure 16: Schematic representation of the SAXS measurement setup. The azimuthal angle φ and radial vector *q* are indicated on the 2D detector. Used with permission from Ref. [45]; permission conveyed through Copyright Clearance Center, Inc.

The result of a SAXS measurement is displayed on the detector as a 2D scattering pattern (Figure 17). When the particles in a sample are randomly oriented, such as dilute dispersions or crystal powders, the scattering pattern has equal intensities along concentric circles around the incident beam. When the sample is partly oriented, like fibres of sheared liquids, intensity modulations can be seen. When the sample is a single crystal with a specific orientation with respect to the incident beam, intensive spots can be observed on the scattering pattern. To analyse the scattering patterns, the intensity is usually integrated over the *q*-vector and plotted as a radial profile of the SAXS pattern. If single, intensive spots are visible on the 2D scattering pattern, it might be useful to integrate the intensity along the azimuthal angle φ, thus creating an azimuthal profile of the SAXS pattern.
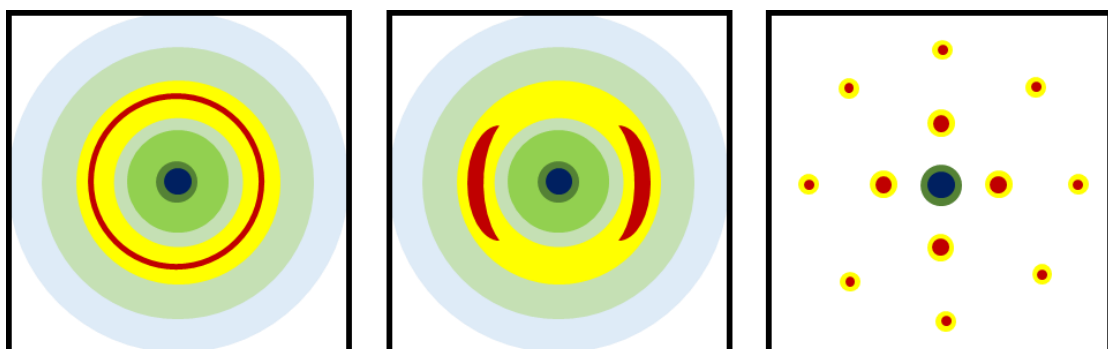

Figure 17: Typical 2D SAXS patterns for a polycrystalline material (left), a textured material (middle) and a single crystal (right).

To determine the amount of certain substances in the sample, the transmission of the material is measured. It is described as the ratio between the intensity of the beam I_0 and the intensity that arrives at the detector I_1, and can be described using the following formula:

$$t = \frac{I_1}{I_0} = exp(-\mu d)$$

(14)

With the absorption coefficient μ and the thickness d of the material.

Normally, the detector cannot withstand the direct beam. Thus, a beamstop is necessary and the intensities I_0 and I_1 cannot be determined directly. A possibility to determine the transmission is by using glassy carbon (GC). For that, three scattering patterns must be obtained: the one of only GC, GC in front of the sample and the sample itself. The transmission of the material is then given by:

$$t_S = (\frac{I_{S+GC}}{t_{GC}} - I_S)/(\frac{I_{GC}}{t_{GC}} - I_{EB})$$

(15)

with I_S as the intensity of the sample, I_{S+GC} as the intensity of the sample with GC in front of it, t_{GC} as the transmission of GC, I_{GC} as the intensity of GC alone and I_{EB} as the intensity of the empty beam.

3. Experimental methods

3.1. Investigated materials and samples

The sample was provided as a NC-hexane dispersion by the research group of Maria Ibáñez at the Institute of Science and Technology in Klosterneuburg, Austria (ISTA) (Figure 18).

The PbTe/PbS NCs were synthesised in a two-step procedure. First, PbTe NCs were created by reacting Pb oleate with TOP:Te (Tri-n-octylphosphin telluride) in octadecene. Thereby, particle sizes with exceptionally narrow size distributions (<10%) could be obtained. In a second step, without purifying or exposing the PbTe NCs to air, the sulphur precursor was added to the crude solution containing the PbTe NCs. Afterwards, the temperature was gradually increased from room temperature to 80 °C at 1.7 °C/min. Reaction conditions like temperature and heating rates had to be carefully adjusted to promote the PbS shell growth on the PbTe core surface [3]. The PbTe/PbS nanoparticles were then dispersed in hexane with a concentration of 5 mg/mL.

Figure 18: Investigated NC-hexane dispersion.

Three samples were prepared from this dispersion, depending on the instrument they were to be measured in, and the self-assembly condition to be studied. First, we wanted to gain information about the nanoparticles themselves, specifically their chemical composition and crystal structure. For this purpose, a drop of the NC dispersion was cast onto a sample holder. After evaporation of the solvent hexane, the remaining dry layers of NCs were measured using XRD. A second sample was prepared in the same way to measure larger superstructures using SAXS.

In another SAXS experiment, we measured the *in-situ* supercrystal growth and final superstructures by examining slow and controlled crystallization through solvent into non-solvent diffusion. All samples were later investigated under a ZEISS Axio light microscope.

3.2. Evaporation of the solvent

For the XRD experiment, a large drop (~ 200 µL) of the NC dispersion was cast on a zero-background sample holder. As soon as the hexane evaporated, the sample was placed into the diffractometer. The XRD measurements were carried out with a D8 Advance Eco (Bruker ASX) instrument equipped with a Cu-Kα X-ray sealed tube (40 kV, 25 mA, λ = 0.154 nm) and an energy-sensitive detector (LYNXEYE-XE). The angle 2θ was set between 10° and 110°, the step size between measurements was 0.02° and the exposure time (duration of one measurement) was 20 seconds.

To measure the superstructures governed by evaporation of the solvent in SAXS, a mixture of ratio 1:10 NC dispersion to pure hexane (~50 µm in total) was cast onto a small glass plate. After a few seconds, as the solvent evaporated, the sample was put into the sample holder and measured in the SAXS instrument (Bruker N8 Horizon) at the Institute of Physics at Montanuniversitsaet Leoben (Figure 19). Cu-Kα radiation with an energy of 8 keV and a Vantec 2000 area detector was used. The sample chamber was held under vacuum at 0.1 mbar to reduce air scattering. The measurements were carried out at a sample to detector distance of 67 cm and covered a *q*-range of up to 5 nm^{-1}, which is optimal to obtain structural information of 100 - 300 nm-sized crystals.

Before starting the measurement, the sample-detector-distance was calibrated by measuring the SAXS pattern of silver behenate (AgB), a material with known peak positions. Afterwards, the specimen was placed into the SAXS instrument, where a 2D scan over the whole sample (exposure time: 0.5 seconds) was performed. From these measurements, 87 positions with high intensities were selected and measured with an exposure time of 1000 seconds.
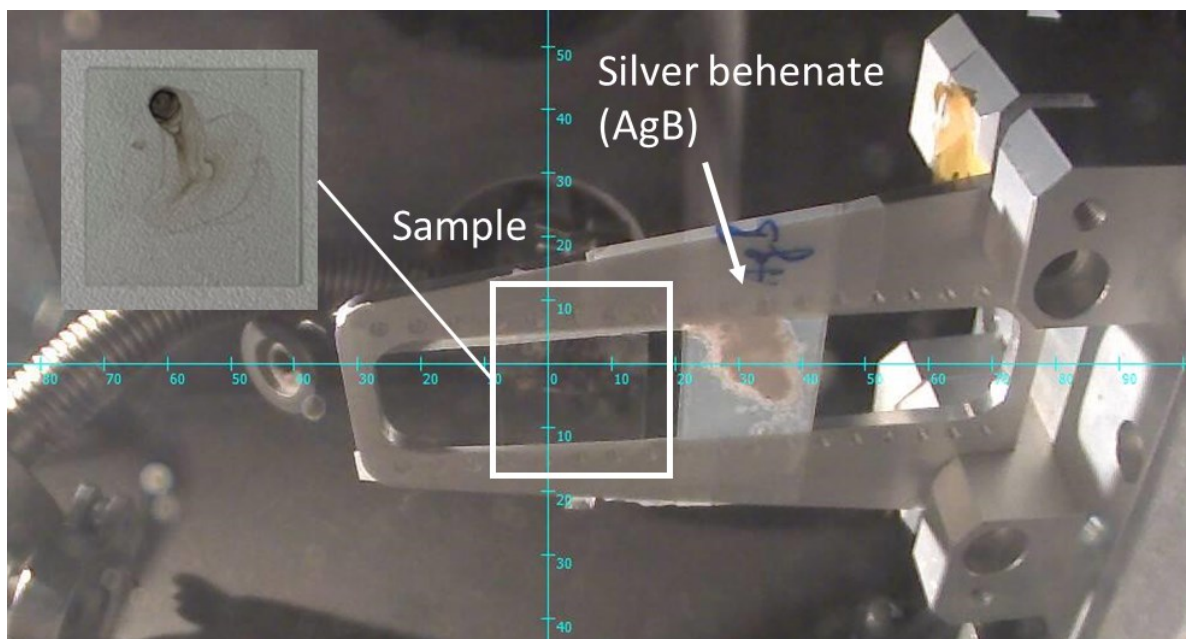
Figure 19: Experimental setup at the SAXS Bruker N8 with an inset of the sample. The X-ray beam is coming from above the sample.

3.3. Solvent into non-solvent diffusion

To study the self-assembly process in situ, a capillary was filled with the non-solvent ethanol and the hexane-nanoparticle dispersion was added on top, at a ratio of 4:3 ethanol to hexane. Then. the capillary was sealed with UV curable adhesive to prevent evaporation of the solvents. To maintain a defined non–solvent–solvent interface, the sample had to be measured in a vertical position, which was only possible at the SAXS instrument NanoStar. First, the sample to detector distance was calibrated by measuring the scattering pattern of AgB. Afterwards, a series of 2D scattering images, as well as the transmitted intensities from about 5 mm above the initial interface (Position 1-10) to 5 mm below (Position 11-19), of the sample have been recorded (Figure 20). The exact locations of the measurement positions relative to the top measurement are summarized in Table 5. To obtain the transmission, GC and the sample with GC were measured with an exposure time of 10 seconds, after each measurement of the sample alone.

The first measurement started at 16:15:00, about 10 minutes after the sample was prepared. I measured from Position 1 to 19 seven times with an exposure time of 100 seconds. A second series of patterns was collected in the same way, while the last three measurement series were obtained at 1000 seconds per measurement. All the measurement series are summarized in

Table 4. Three weeks after the *in-situ* measurements, several *ex-situ* measurements at selected positions were performed with an exposure time of 3600 seconds. During those measurements, the liquid was still present in the capillary (Figure 21). Another few weeks later, when the liquid has already evaporated through a hole in the adhesive, several measurements were taken at positions where we believed to find supercrystals.
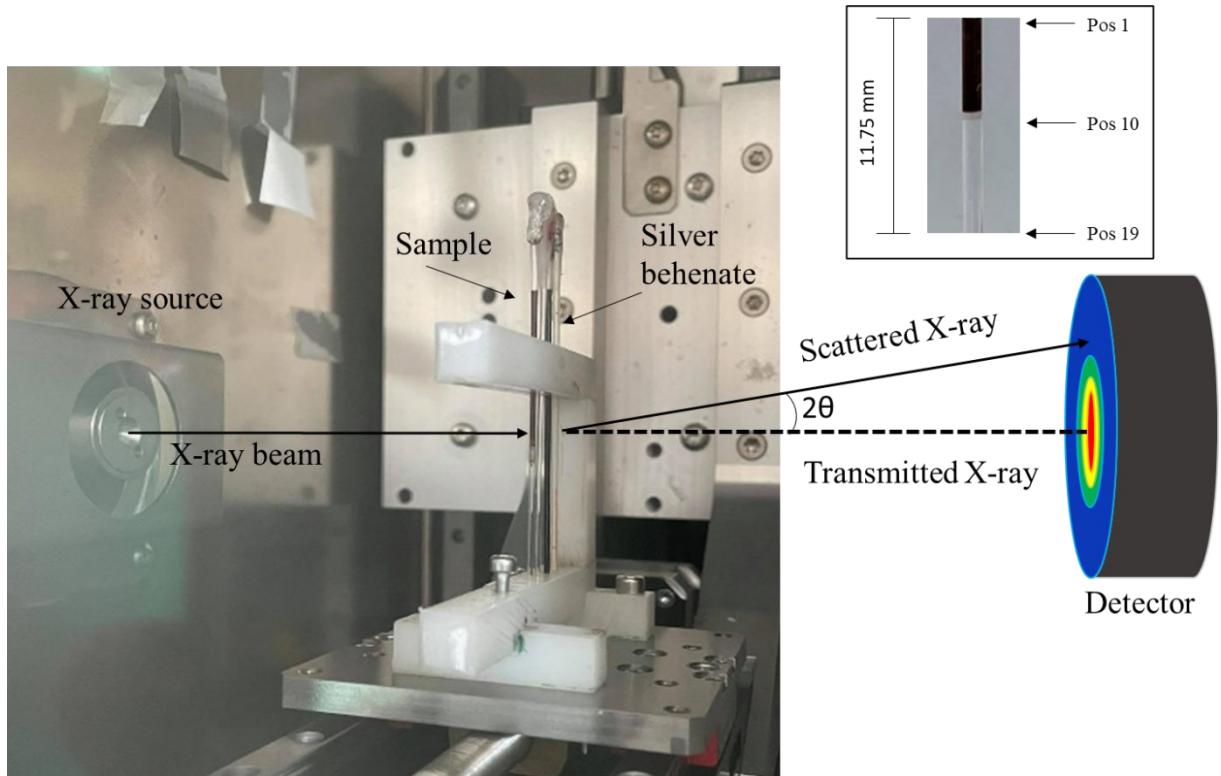

Figure 20: Experimental setup at the SAXS NanoStar with a close-up of the non-solvent solvent interface in the capillary.

Table 4: Overview of all *in-situ* SAXS measurements.

Measurement series	Start date [dd.mm.yyyy]	Start time [hh:mm:ss]	Number of measurements (only sample)	Exposure time [s]
1	21.04.2021	16:45:10	133	100
2	21.04.2021	22:27:52	133	100
3	22.04.2021	12:22:44	19	1000
4	22.04.2021	18:05:00	114	1000
5	24.04.2021	15:27:06	114	1000

Table 5: Exact positions of the measurements, starting from the top measurement at 0 mm.

Position No.	Position [mm]
1	0
2	1
3	2.25
4	3
5	3.5
6	4
7	4.5
8	5
9	5.5
10	5.75
11	6.25
12	6.75
13	7.25
14	8
15	8.75
16	9.5
17	10.25
18	11
19	11.75
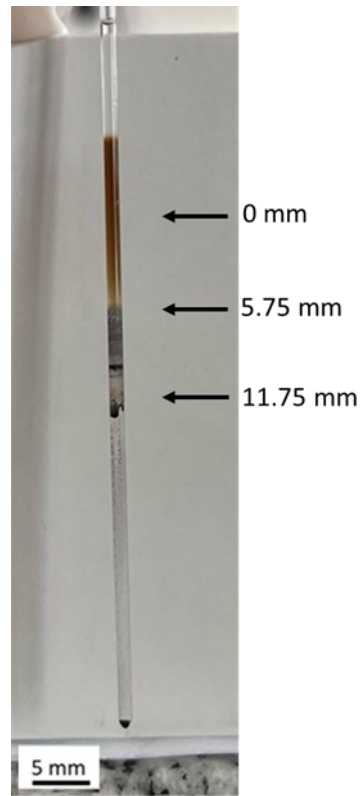
Figure 21: Sample after the *in-situ* SAXS measurements.

4. Data analysis

The obtained 2D patterns were viewed and edited using the MULIP SAXS-2D software [26]. Before every data evaluation, the AgB measurement was loaded, and the software calculated the exact sample-detector-distance from the centre positions of the silver behenate rings. The radial profiles were obtained by masking unwanted regions and integrating the 2D patterns over 360°. To obtain the intensities and locations of the distinct spots, the patterns we integrated along the azimuthal angle φ.

The transmission correction was carried out using a Matlab script written by R.T.Lechner. The program calculated the transmission using equation (15), with the transmission of glassy carbon as 0.16 [27] and the intensity of the empty beam as 0.006. For the transmission correction of the SAXS data, the intensities of the sample were divided by the transmission values.

To obtain structural information from diffraction peaks, they are approximated using the Gauss function.

$$G(x,y) = \frac{1}{2\pi\sigma^2} e^{\frac{x^2+y^2}{2\sigma^2}} \tag{16}$$

There is a correlation between the number of unit cells N (= size of the crystallite) and the full-width-half-maximum (FWHM) of the Gauss function. It is explained by the Scherrer equation, which states that a broadening of the diffraction peak depends on the size of coherently diffracting domains (Figure 22). The crystallite size can be described using the FWHM or the standard deviation σ.

$$FWHM = \sqrt{2\,ln2} \cdot \sigma \tag{17}$$

$$SC = \frac{2\pi K}{FWHM} \tag{18}$$

K is a dimensionless shape factor, which is typically close to one [28].

A method to obtain a more accurate value of the crystallite size, than by solely applying the Scherrer equation, was proposed by Williamson and Hall. It states that the crystallite size, as well as microstrain broadening, vary with respect to the Bragg angle θ:

$$FWHM \times \cos\theta = \underbrace{\frac{K\lambda}{SC}}_{\text{y-intercept}} + \underbrace{4 \times Strain \times \sin\theta}_{\text{slope}} \qquad (19)$$

This equation is equivalent to the standard equation of a straight line, $y = kx + d$ (k = slope, d = y-intercept). By plotting the FWHM versus $\sin\theta$ we obtain the size component from the y-intercept of the slope [29].
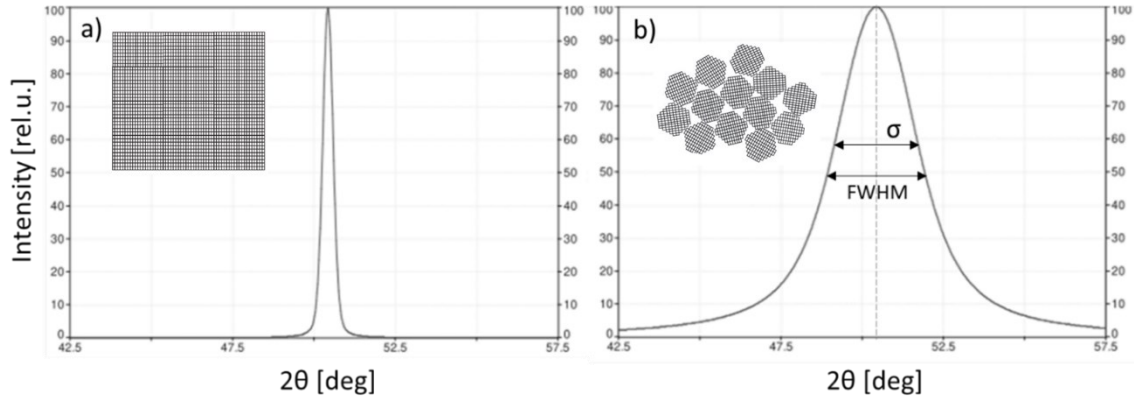

Figure 22: Typical Gaussian peak shapes of a) a perfect single crystal and b) a nanocrystalline assembly [46].

In this work, MATLAB [30] and Fityk [31] were used for processing the SAXS data. First, the constant background was removed, and then the peaks were fitted using the Gauss function (Figure 23). From their FWHM and centre positions, it was possible to determine the supercrystal sizes and the d-spacings between the lattice planes. The lattice type was determined from the centre positions of the Gauss peaks.

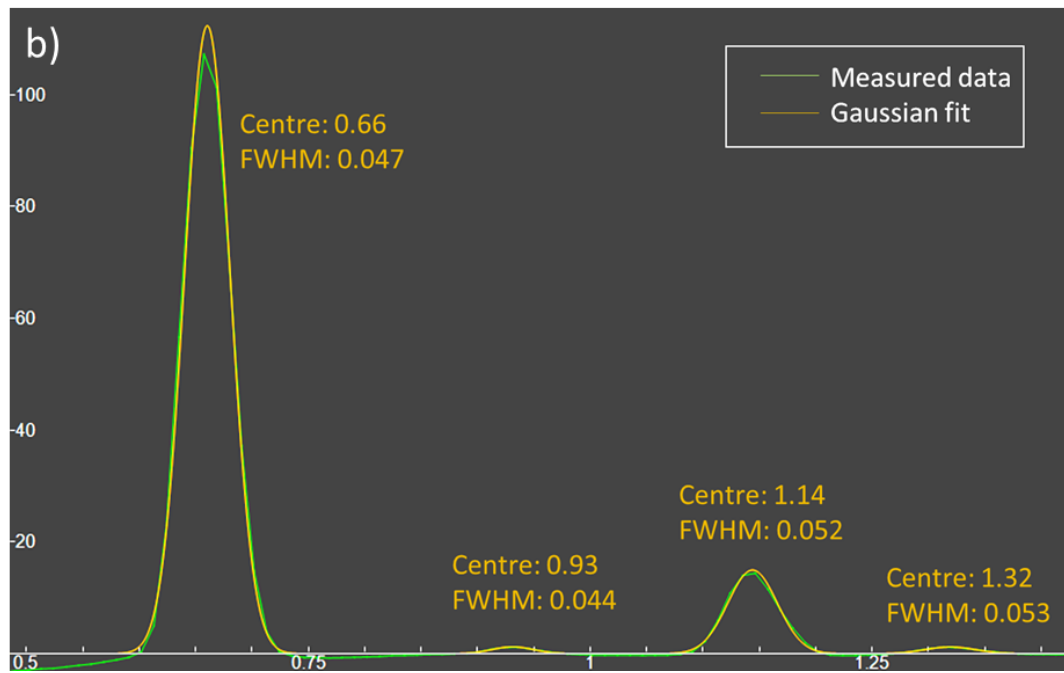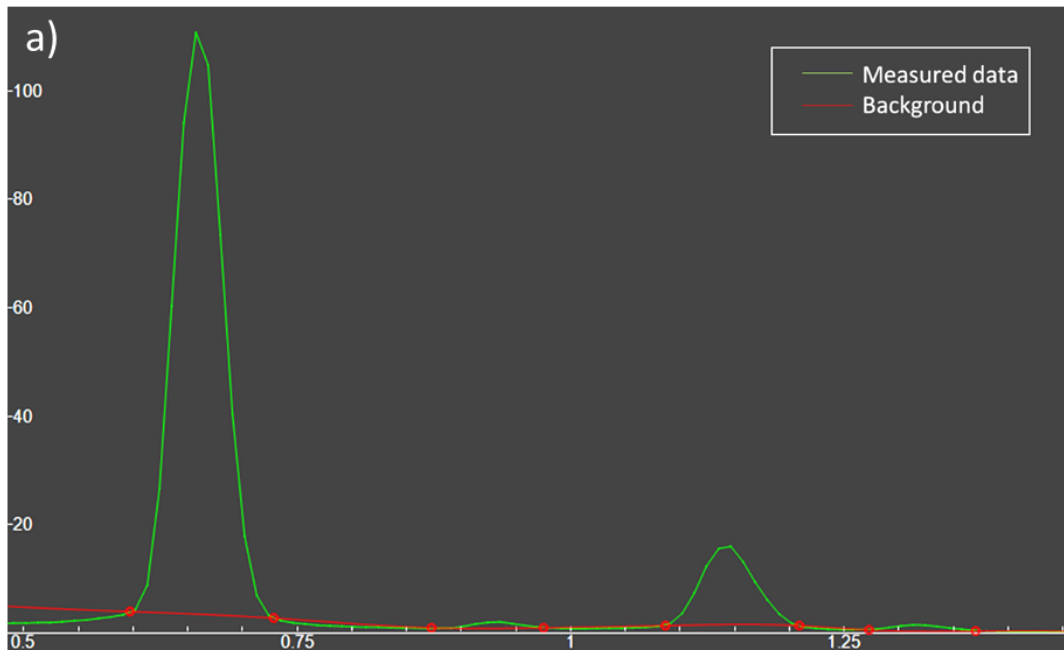Figure 23: SAXS data and a) background correction, b) Gaussian fits, displayed with Fityk [31].

5. Results and discussion

In the following chapters, the data obtained in the described experiments will be presented and analysed.

Chapter 5.1. will focus on the information that could be gained from the NCs which remained on the substrate after evaporation of the solvent. From the XRD measurement, we were able to determine their crystal structure, while the SAXS data gave insight into the NCs' shape and the superstructures they assembled to.

The SAXS data obtained from the diffusion of a non-solvent into the NC-hexane dispersion will be analysed in Chapter 5.2. The shape of a single NC, previously obtained by a shape retrieval method developed in a paper from M. Burian and Rainer T. Lechner [32], will be correlated with the investigated superlattices, showing the exact alignment of the NCs in the supercrystal. The superstructures will be analysed depending on the measurement position relative to the initial interface between solvent and non-solvent. In the end, the results from both mechanisms will be summarized and compared.

5.1. Evaporation of the solvent

5.1.1. Structure of the nanoparticles

The nanoparticles that remained on the sample holder after evaporation of the solvent have been investigated with XRD. The observed XRD pattern is presented in Figure 24.

The centre positions of the first two peaks, remarkably higher than the following ones, fit the theoretical peak positions of the fcc (200) and (220) peaks of PbS and PbTe. The reason for this high difference in peak maxima could be that the particles are not perfectly spherical but have facets. Therefore, the NCs probably have aligned in thin films and tend to be oriented along the (200) and (220) planes, which are indicated in Figure 25.

The structural parameters of the NCs calculated from the peak positions and widths are summarized in Table 6 and Table 7. From the FWHM, the mean size of the core was determined to be 3.0 ± 0.7 nm, which is slightly lower than its theoretical size of 7 nm (Figure 25) [8]. External factors (stacking faults, crystal defects etc.) may increase the peak width, thus the size determined might be smaller than the actual size of the NCs. The diameters of the core and shell

slightly vary because the penetration length of the X-ray though the particles varies depending on the incident angle of the beam. From the XRD data, no sign of an overall asymmetric shape, as has previously been described in literature [3,32], could be determined. The Scherrer equation only gives accurate solutions for spherical particles, and since the shell is rather a hollow sphere, its size cannot be determined accurately using this method. The calculation would require further detailed studies in this field, which would go beyond the frame of this thesis. Nevertheless, an approximate value of 2.8 ± 0.4 nm for the shell size was obtained using the Scherrer equation, which is close to the theoretical shell size of 3.4 nm (Figure 25).
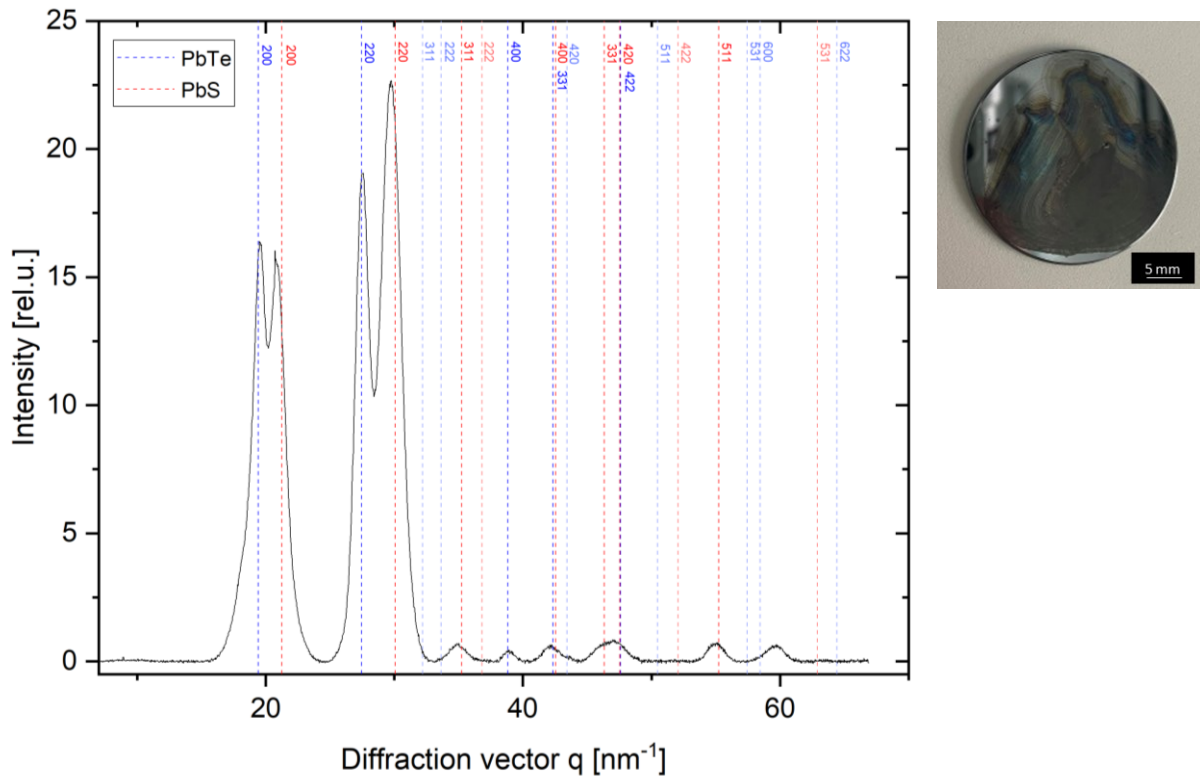

Figure 24: XRD pattern of the sample which is shown on the right. The vertical red lines indicate the theoretical peak positions of PbTe (blue) and PbS (red).

Table 6: Obtained structural parameters of the PbTe core ($a = 6.47$ Å) [33].

q [nm^{-1}]	19.4	27.5	32.2	33.6	38.9	Mean
(*hkl*)	(200)	(220)	(400)	(331)	(422)	
d-spacing [nm]	3.2	2.3	1.6	1.5	1.6	
SC size [nm]	2.6	3.7	4.1	2.6	2.3	3.0 ± 0.7

Table 7: Obtained structural parameters of the PbS shell (a = 5.91 Å) [33].

q [nm^{-1}]	21.3	30.1	35.3	42.5	46.3	47.6	55.2	Mean
(*hkl*)	(200)	(220)	(311)	(400)	(331)	(420)	(511)	
d-spacing [nm]	3.0	2.1	1.8	1.5	1.4	1.3	1.1	
SC size [nm]	3.6	2.5	2.9	2.6	2.9	2.3	2.5	2.8 ± 0.4

The different structures, the PbTe/PbS NC assembled to, are visible in the light microscope (Figure 26). The colourful lines, which may confirm the particle assembly in a form of thin layers, remind us of oil spots in water. The light that hits the sample consists of multiple colours, all waves with different wavelengths. If two diffracted light beams, one from the surface and one from the bottom of the layer, interfere, some colours may be enhanced, while others may vanish. The visible colours depend on the wavelength of the beam, as well as on the thickness of the layer. If too many particles to form layers are present, they tend to agglomerate to dark brown spots instead. Especially in the middle of the substrate, the number of NCs is high, because during the evaporation process, the dispersion is concentrated in one spot. A few small assemblies of agglomerated particles are visible on the thin NC layers, as marked in Figure 26 (c). Except for the colourful layers of NCs, no ordered superstructures are visible in the microscopy images.

Through the XRD experiments, we were able to verify, that the particles consist of PbTe and PbS. The calculated sizes of the core and shell are very close to the theoretical sizes, but a more accurately calculated shape from SAXS data will be presented in Chapter 5.2.1. Even with XRD, we could assume that the particles are not perfectly spherical but have certain facets. The superlattice resulting from evaporation of the solvent shall be presented in the next section.
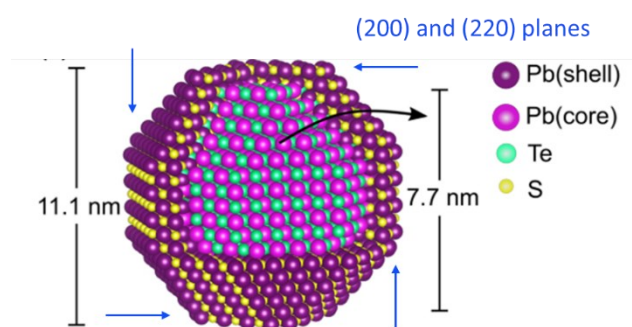

Figure 25: Schematic illustration of a single NC with the theoretical diameter of only the PbTe core (7.7 nm) and including the PbS shell (11.1 nm). The blue arrows mark the (200) and (220) facets of the NCs. Reprinted with permission from Ref. [8]. Copyright 2020 American Chemical Society.
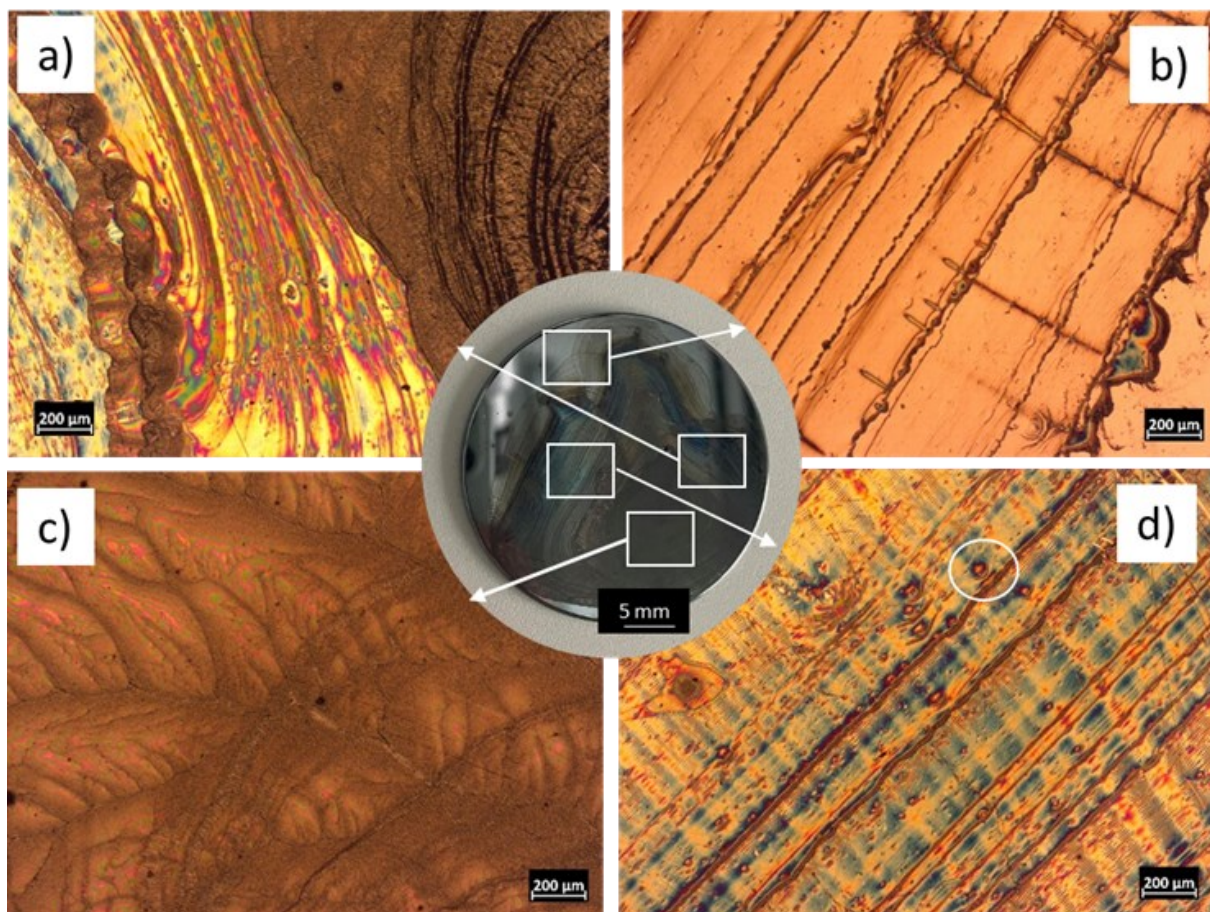
Figure 26: Microscopy images of the XRD sample at different locations on the sample, which are indicated on the image of the sample inserted in the middle. In a), colourful layers and brown spots of agglomerated NCs are visible. The thin lines in b) are present at the corner of the specimen and remind of coffee rings. c) shows a close-up of the brown structure in the middle of the sample, while in d) thin layers of NCs, as well as a few spots of agglomerated particles, like the one marked in white, are visible.

5.1.2. Superlattice

To examine the overall superstructure the NCs assembled to in the scenario of solvent evaporation, another sample has been prepared and observed in the SAXS instrument (Figure 27). Since the X-ray must pass through the sample, the sample must be able to transmit as much light as possible. In this case, a very small amount of the NC dispersion was cast onto a glass substrate.
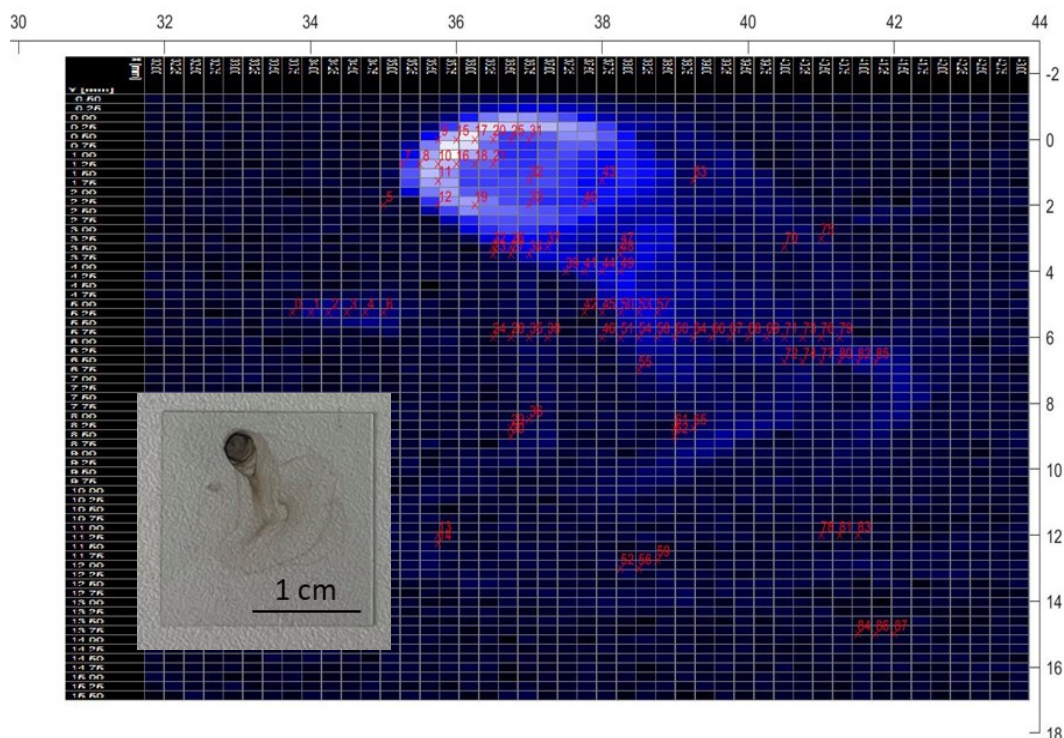
Figure 27: 2D scan over the whole sample, with an exposure time of 0.5 seconds. Lighter spots indicate higher intensities. The positions which were later measured with a higher exposure time, are marked in red. For comparison, a photography of the sample is shown on the lower left.

The SAXS measurements revealed that through evaporation of the solvent hexane, the NCs self-assembled to a body-centred cubic (bcc) crystal structure (Figure 28). The peak intensities also correspond to the theoretical intensities of the bcc peaks, considering the form factor of the dispersed NCs (Chapter 5.2.1., Figure 36) and the multiplicity factors of the bcc lattice (Table 3). In the radial profiles plotted in Figure 28, the q-positions of the maxima are equal, which means that the particles assembled to the same lattice, with the same dimensions. They are solely distinguishable by their peak intensity and width, which is an indicator for different crystallite sizes. Using the parameters given in Table 1, the d-spacings of the bcc (110) planes, the lattice constants a and the particle diameters D were determined. The supercrystal sizes for the four positions shown in Figure 28 were calculated using the Scherrer equation. The obtained results are presented in Table 8 and Table 9.

Table 8: Obtained lattice parameters from *q*-positions in Figure 28.

q [nm^{-1}]	(*hkl*)	*d* [nm]	*a* [nm]	*D* [nm]
1.11	(110)	5.7	8.0	6.9
1.57	(200)	4.0	5.7	4.9
1.92	(211)	3.3	8.0	6.9
2.22	(220)	2.8	6.3	5.4
Mean				6.0 ± 0.9

Table 9: Supercrystal sizes obtained for the positions in Figure 28.

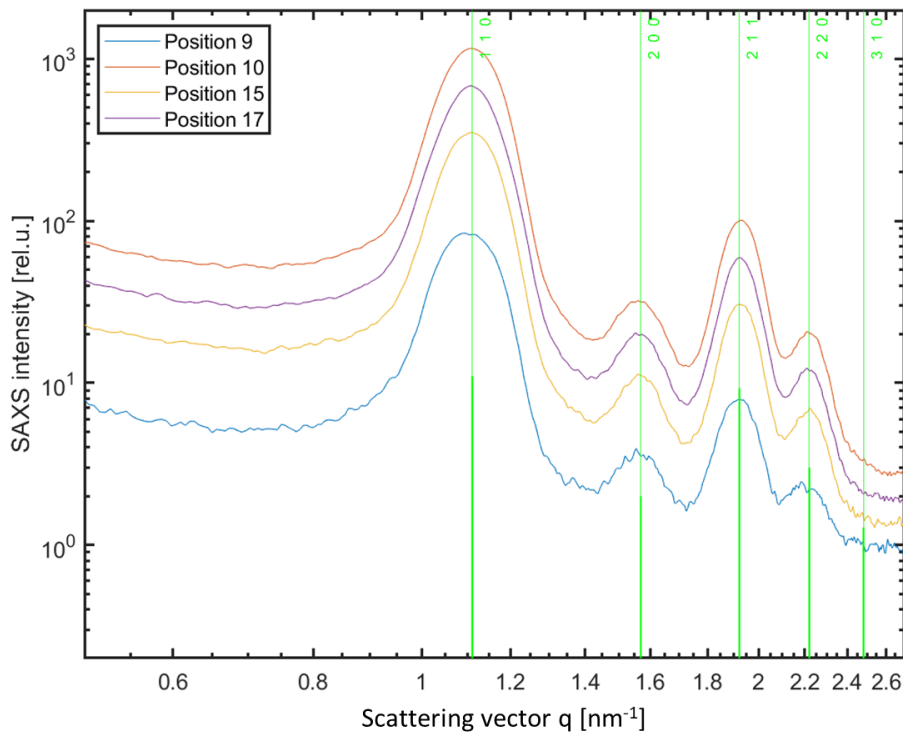| Position	SC size [nm]
9	40.4
10	35.3
15	43.2
17	45.5
Mean	41.1 ± 3.8
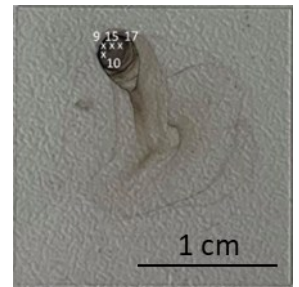
Figure 28: Radial profiles at positions with high intensities. The green lines indicate peak positions of the bcc lattice at *a* = 8 nm, thicker lines indicate the theoretical intensities of the peaks, calculated by removal of the form factor of the dispersed NCs and multiplication with the multiplicity factor *m* for the bcc lattice. The sample with the locations of the presented positions is shown on the right.

Considering the diameters of the core and shell (~11.1 nm) given in literature [8], the SC structure is very dense, as the diameter D of the NCs in the measured bcc lattice is 6.0 ± 0.9 nm. This narrow structure may arose from the quickly evaporating solvent, which enabled the particles to align as close as possible (Figure 31). The 2D patterns show rings with a slightly changing intensity along the azimuthal angle. This might indicate that the SCs are oriented along certain planes, but they might also be random fluctuations (Figure 29).

In the images created with an optical microscope, structures reminding coffee rings stand out (Figure 30 a). During the evaporation of the solvent, the particles moved to the perimeter of the drop and dense rings of solid material remain. Similar rings were also visible on the XRD microscopy images (Figure 26 b).
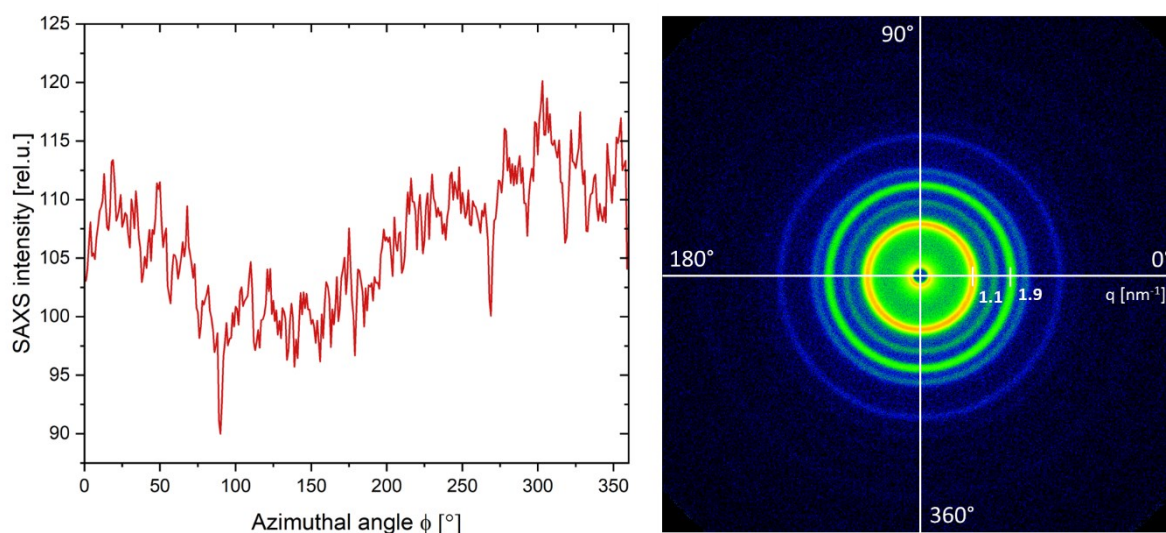

Figure 29: On the right side, a 2D SAXS pattern taken at position 10, is shown. The corresponding azimuthal SAXS profile, integrated over all rings, is presented on the left. A decrease in intensity is visible near 90°, which indicates that the SCs are oriented along certain, preferred directions.

No colourful layers are visible here, as we saw before in Figure 26. This can be explained by the much smaller amount of liquid used here. Due to minimization of surface energy, particles usually tend to aggregate into dense structures, rather than form thin layers. So, at a sufficiently high quantity of particles, they can form layers, but if the concentration of NCs is too low, they rather assemble to dense and ordered structures. Generally, particles move very quickly during the evaporation process, which makes it difficult for them to align into ordered crystalline structures. The self-assembly process can be slowed down in this case, if the number of particles is reduced. At higher magnifications, distinct crystalline structures, which remind of dendrites, become visible (Figure 30 b and c). They are located at spots where no coffee rings exist, with

even concentrations of nanoparticles. It seems, that the concentration of nanoparticles in this sample is low to enable a slower and more controlled evaporation than on the XRD sample.
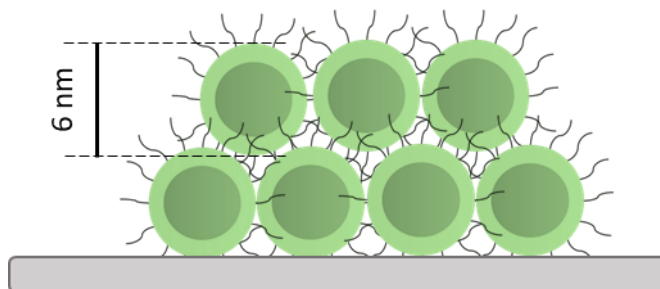

Figure 31: Layers of NCs on the substrate, assuming perfectly spherical particles.
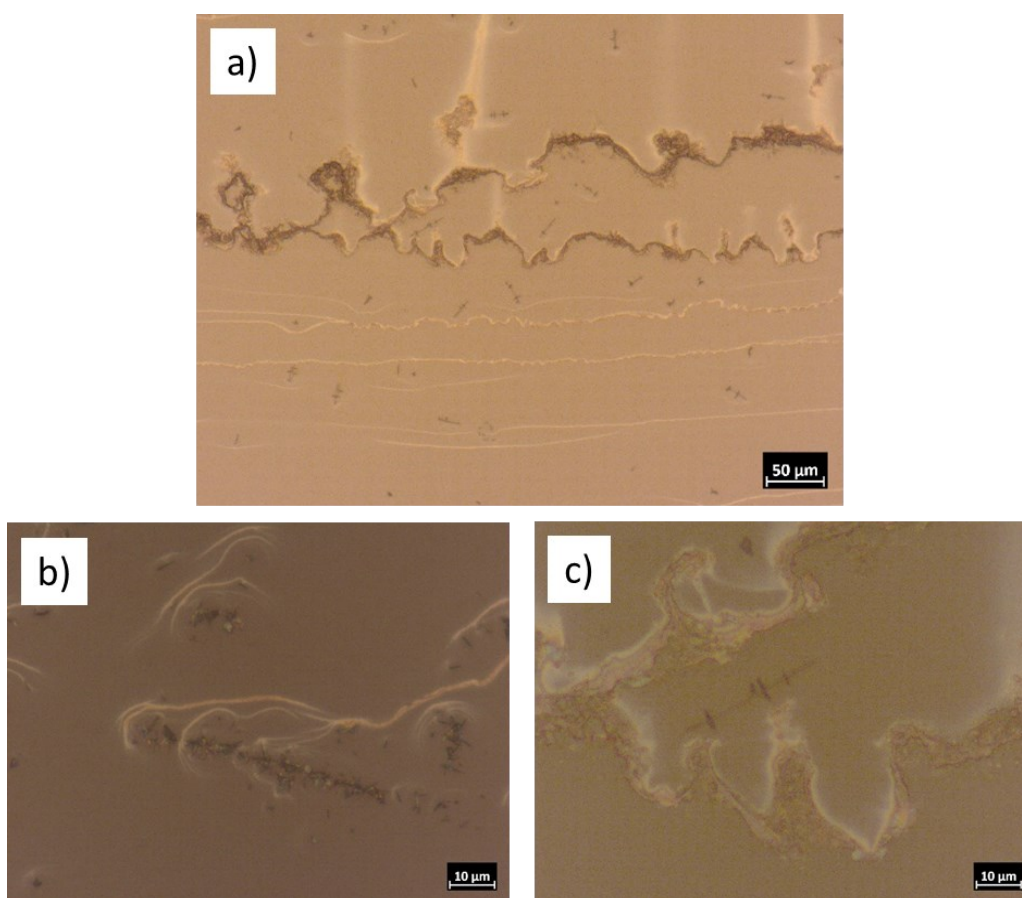

Figure 30: Microscopy images of the sample. At small magnifications (a), the coffee rings are visible, at larger magnifications (b) and (c) we see small, elongated structures.

In summary, the technique to obtain supercrystals through evaporation of the solvent is very quick and easy, which can become useful in large-scale production. But the downside of this process is, that the concentration of NC needs to be very low to achieve ordered superstructures. A very dense bcc structure has been achieved by this method, with the ligands being pressed together closely, which can be beneficial for properties like electrical conductivity. Hoping to

achieve larger and more ordered superstructures, a second method was applied: the diffusion of a non-solvent into the NC dispersion. The results obtained by this technique will now be presented.

5.2. Solvent into non-solvent diffusion

The diffusion of the non-solvent ethanol into the NC-solvent mixture was observed *in-situ*. Although the densities of hexane and ethanol are different (Table 10), the two solvents are miscible. The reason for that is that ethanol is a polar molecule because its hydroxyl group is more dominant than the non–polar hydrocarbon end (Figure 32). That non-polar end allows it to have a certain level of miscibility with the non-polar hexane [34]. The high density of PbS and PbTe leads to the diffusion of nanoparticles downwards and the mixing of ethanol and hexane.
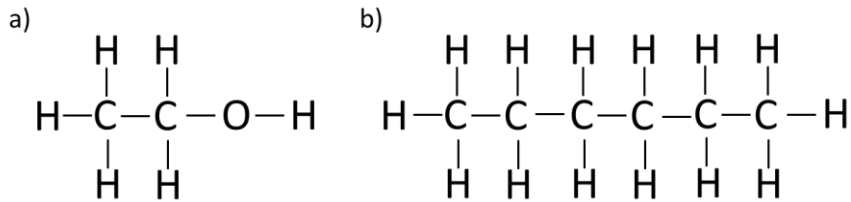
Figure 32: Structural formula of a) ethanol and b) hexane.

A convenient way to get an overview of all processes happening in the capillary is to divide it into three areas: (1) above the initial interface, where diffusion of ethanol into the NC dispersion takes place, (2) below the interface, where the SCs from the interface fall into the solvent ethanol and (3) at the interface, where both mechanisms occur simultaneously. Those areas will first be treated separately and later summarized.

The obtained radial SAXS profiles show distinct peaks with similar sizes and shapes at almost every position, thus indicating similar crystalline structures along the entire capillary (Figure 33 a). In Figure 33 b), a change of the *q*-positions along the capillary is visible. They slightly increase at the initial interface, after rapidly decreasing below. As the *q*-values are indirectly proportional to the *d*-spacing according to equation (13), the *d*-spacings are lowest at the interface, which means that here the structure is the densest. Additionally, the highest peak intensity, and therefore the highest number of particles, was measured at the interface (Figure 33 c). We can therefore assume that due to the supersaturation conditions, caused by the high concentration of non-solvent at the interface, here the NCs tend to self-assemble into denser structures. Despite the high number of SCs measured here, most of the NCs assembled to large

agglomerates and dropped to the bottom of the capillary, which can be seen in the photography of the sample after the experiments (Figure 21 and Figure 34).

The closer we get to the interface, starting from far inside the NC dispersion, the earlier the crystallization process sets in (Figure 34). This can be expected because the non-solvent ethanol is responsible for the attraction between particles and the start of crystallization, so as soon as it reaches a certain position, the crystallization process can start. In this experiment, the measurements were running during the first 10 hours and only continued the next day, 10 hours later. Therefore, we had no information about what was happening between hour 10 and hour 20 of the *in-situ* diffusion process. By approximating the points of the start of crystallization with a polynomial fit, the theoretic starting points in this missing time frame have been estimated. By performing a linear fit of the curve in Figure 34 we discovered that the rate, at which crystal growth begins, is approximately 0.3 mm/h. With this information, it is possible to estimate, how long one must measure the *in-situ* diffusion to follow the crystallization up to a given height above the interface.
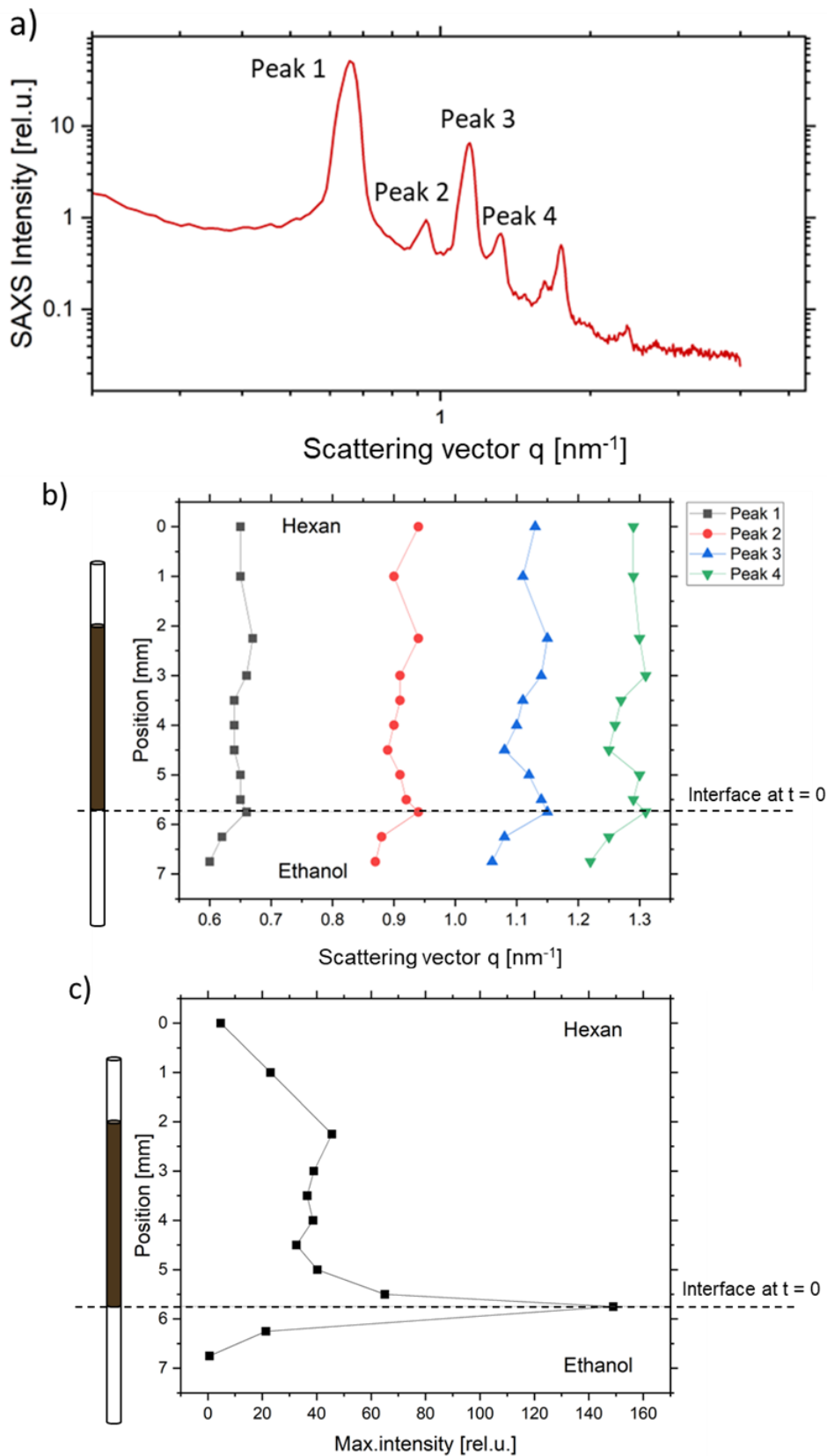
Figure 33: Overview over the obtained scattering data at all positions. a) represents a radial SAXS profile. Similar patterns were observed at all positions. b) shows the change of centre positions of the four peaks indicated in a), depending on the measurement position on the capillary. The maximum intensity of Peak 1 is presented in c), with a high increase in intensity at the initial interface.
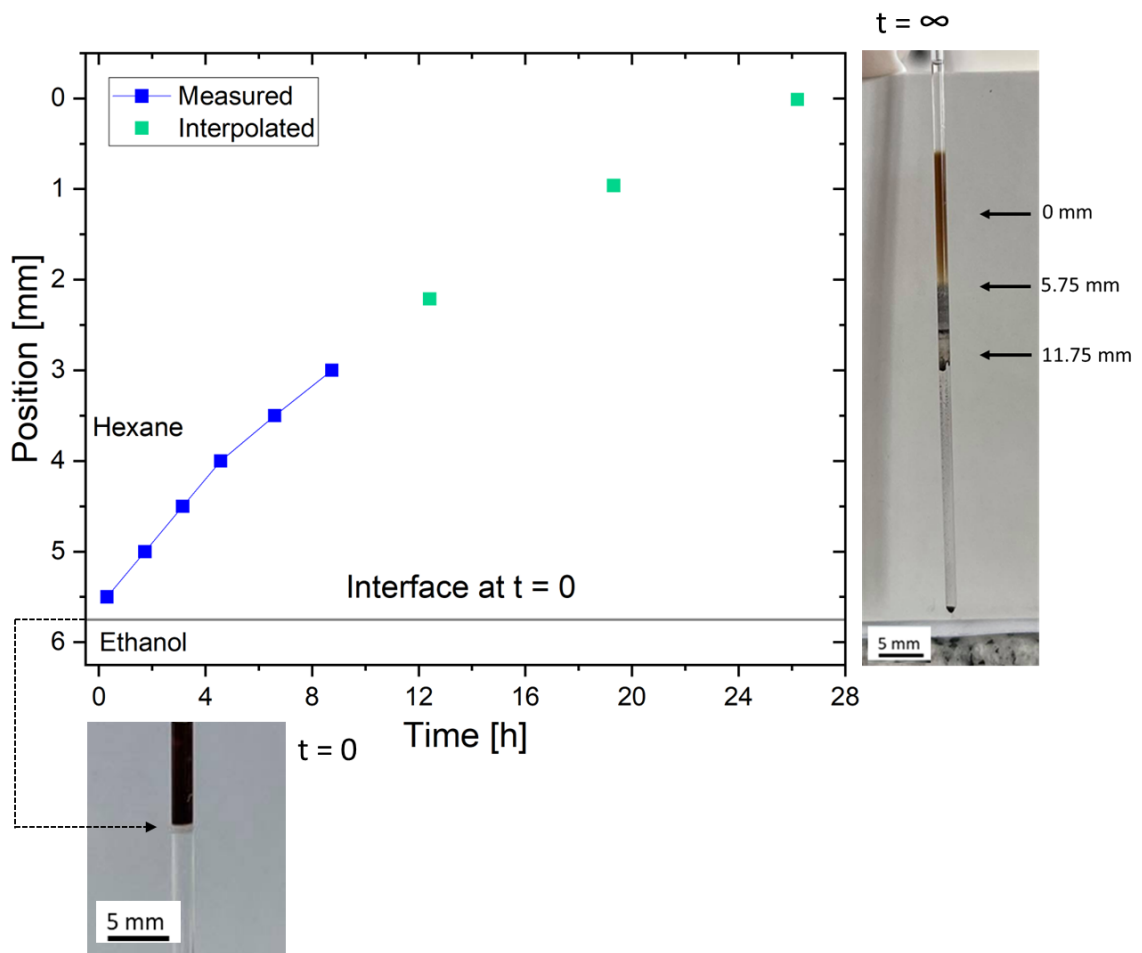
Figure 34: Time when the first crystalline peak appears, at all positions. The further we go upwards into the NC dispersion, the later the first peak appears. Below the interface, the peaks are present at t = 0, the further into the NC dispersion, the later the peaks appear.

As stated in the experimental section, the transmission during the *in-situ* diffusion process was measured simultaneously. If we look at Figure 35, we see a gradual increase in the transmission along the measured positions, at the beginning of the measurement (t = 0 h), with a sudden jump at the interface. This can be explained by the decreasing concentration of nanoparticles at positions far above the interface, as they are slowly diffusing downwards. In Table 10, the calculated transmission values were compared to the expected theoretical values at selected positions. For example, the transmission of hexane and glass is 0.6, but the transmission measured at 0 mm at t = 0 h, where we expect hexane and glass, is much lower (0.14). From this difference in transmission values, the transmission of the dispersed NCs, and therefore their concentration, could be determined by applying equation (14). At the beginning of the measurement, we expect pure ethanol below the interface. The transmission values are around 0.3 - 0.4, which is slightly lower than the calculated value for the transmission of ethanol and

38

glass. This difference might have been caused by light deflections of the beam during the measurement, which sometimes can happen. Another factor which might influence the measured transmission value is the varying thickness of the capillary. It is assumed that the closer to the bottom, the thicker it gets. The sudden jump in the transmission values close to a time of 10 hours can be explained by the fact that we started a new measurement series here on the next day, so a few hours have passed without measuring the change in transmission. The reason for its increase is the mixing of ethanol and hexane, and due to most nanoparticles dropping down to the bottom of the capillary. If we compare the sample before and after the measurement in Figure 35, the latter one is much more transparent in the upper parts, where NCs are present, than the former.
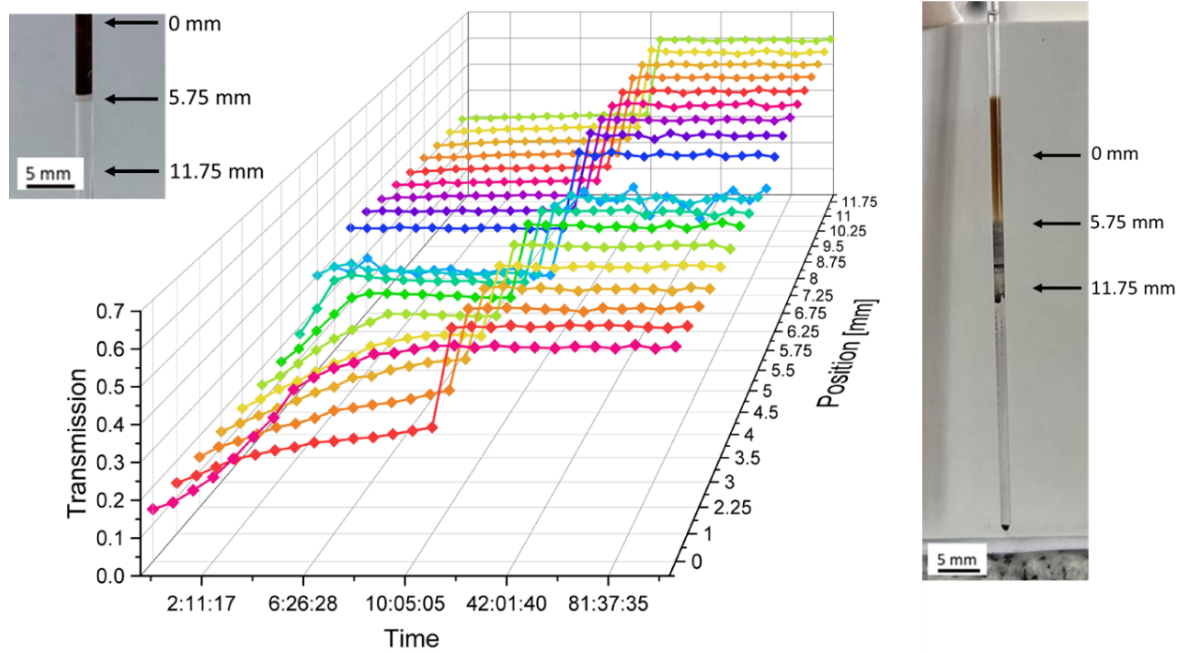

Figure 35: 3D plot giving an overview over all measured transmission values. An image of the sample at the beginning of the measurement is shown on the left, the sample after the measurement is shown on the right.

Table 10: Thicknesses, densities and assumed or calculated transmission values [27], compared to the measured ones.

Substance(s)	Thickness [μm]	Density [g/cm^3]	Theoretic transmission	Measured transmission
Glass capillary (SiO$_2$)	20	2.65	0.8	-
Hexane (C$_6$H$_{14}$)	1300	0.66	0.73	-
Ethanol (C$_2$H$_5$OH)	1300	0.79	0.52	-
PbTe	7*	8.16	0.24	0.24
Hexane and ethanol mixed	1300	-	0.65	-
Glass capillary + hexane	1320	-	0.6	-
Glass + hexane and ethanol 1:5	1320	-	0.46	0.55 - 0.62
Glass and ethanol	1320	-	0.43	0.31 - 0.34
Glass + hexane and NCs mixed	1320	-	-	0.14

*The thickness of PbTe was calculated from the measured transmission.

5.2.1.   Shape of the nanoparticles

The SAXS measurements obtained during the first 10 hours of the measurement, 5 mm above the initial interface, show only the form factor of the dispersed nanoparticles (Figure 36). The intensity is getting smaller with time, which means that the particle concentration is decreasing at the observed position. From similar measurements, the shape and size of the nanoparticles has been previously retrieved using model free shape reconstruction with DAMMIN [35]. This computational method arranges artificial dummy atoms into a 3D shape so that its scattering pattern fits best the measured SAXS data [19]. The reconstruction of the NC shape was performed by M. Burian [36] and plotted with PARAVIEW [37] (Figure 37). The fact that the particle doesn't have a perfectly round shape will be crucial for the following determination of the crystal structure. The previous assumption of rather spherical, faceted particles (Chapter 5.1.2.), is not as accurate as the shape retrieval, and therefore the latter will be used in the further discussion.
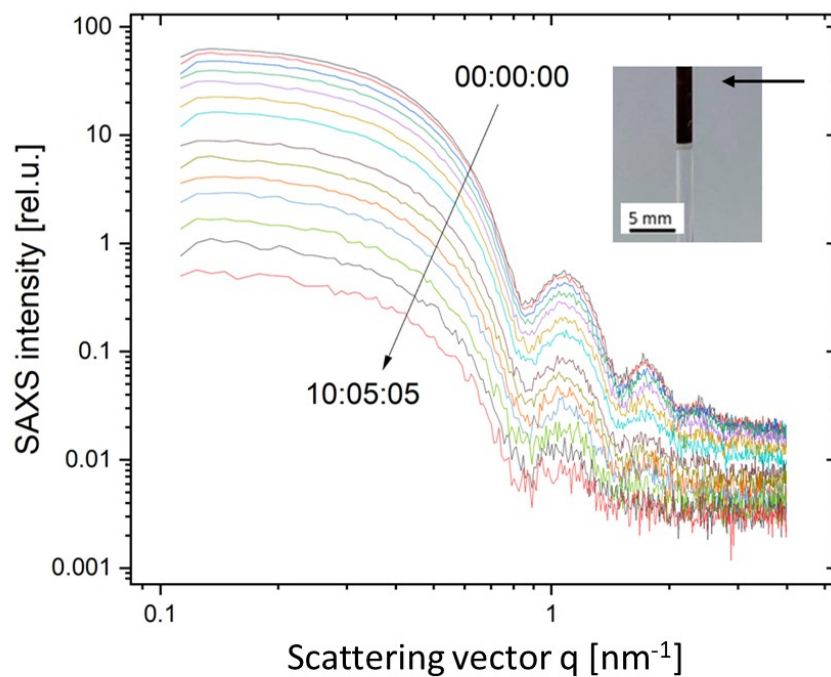
Figure 36: Radial SAXS profile of the NC dispersion above the interface, during the first 10 hours of the *in-situ* diffusion experiment. An image of the sample with the indicated position, where the measurements were taken, is shown on the upper right. Such profiles represent the form factor of the NCs and are used to determine their shapes.
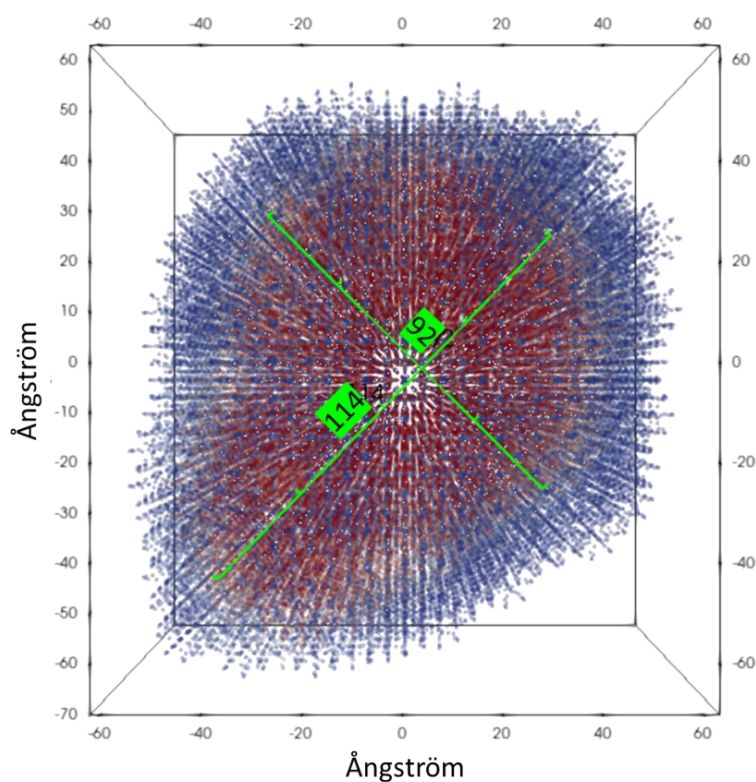

Figure 37: 3D model of the shape of the NC. The colours indicate the probability of occupancy, with red being a high probability and blue being a low probability. The smallest and largest obtained diameters are indicated (92 Å and 114 Å).

5.2.2.   At the interface

At the interface, the transmission values are low at the beginning at get slightly higher towards the end of the measurement (Figure 38 a). This change can be explained by the decreasing number of dispersed NCs and supercrystals at this position. Nevertheless, we observed the largest number of particles at the interface, where the concentration of ethanol, and therefore the diffusion gradient, is the highest. Here, crystallization sets in early, even before the first SAXS measurement has been started. As the measurement and crystallization process continue, the superlattice peaks are moving to higher q- and Intensity values, meaning that the lattice spacings are becoming smaller and the number of supercrystals in the X-ray beam become larger (Figure 38 b).

The SAXS profiles taken at the interface indicate a body-centred cubic structure (Figure 39 a). The 2D plots show multiple rings with high intensities due to the high number of differently oriented supercrystals in the X-ray beam (Figure 39 b).
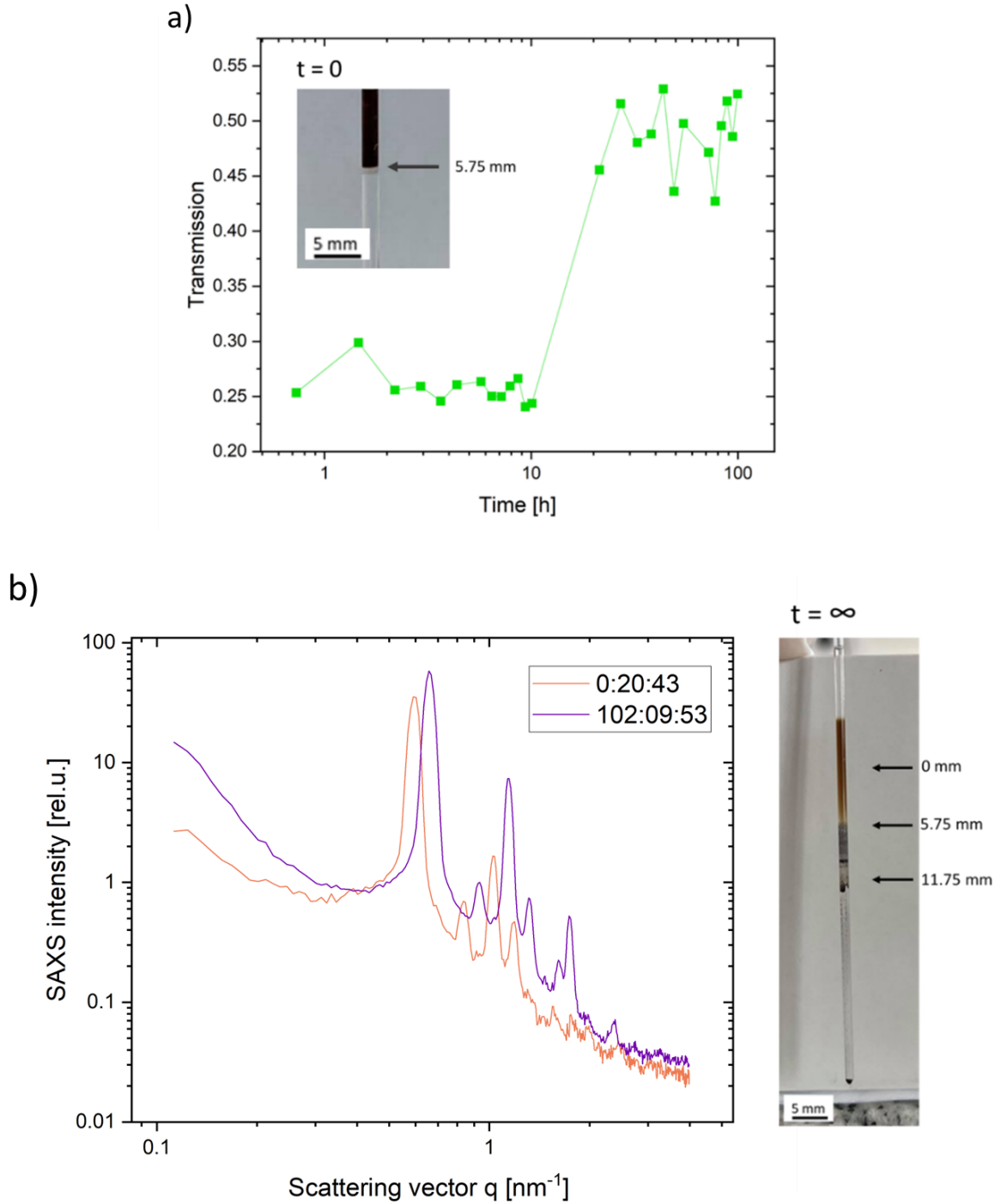
Figure 38: a) Transmission values, with an inset of the capillary at the beginning of the measurement, indicating the interface, and b) 2 radial SAXS profiles, one at the beginning and one at the end of the measurement, measured at 5.75 mm below the top measurement (0 mm). The measurement positions are indicated on the image of the capillary at the end of the measurement, shown on the right.
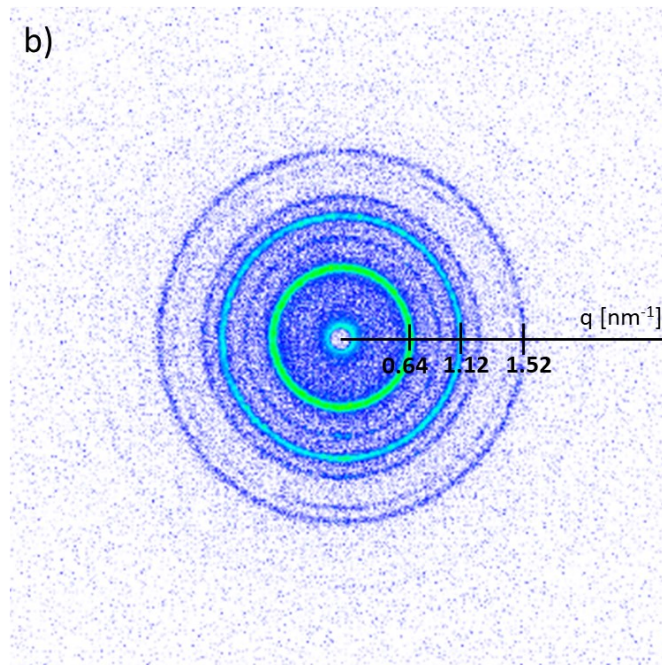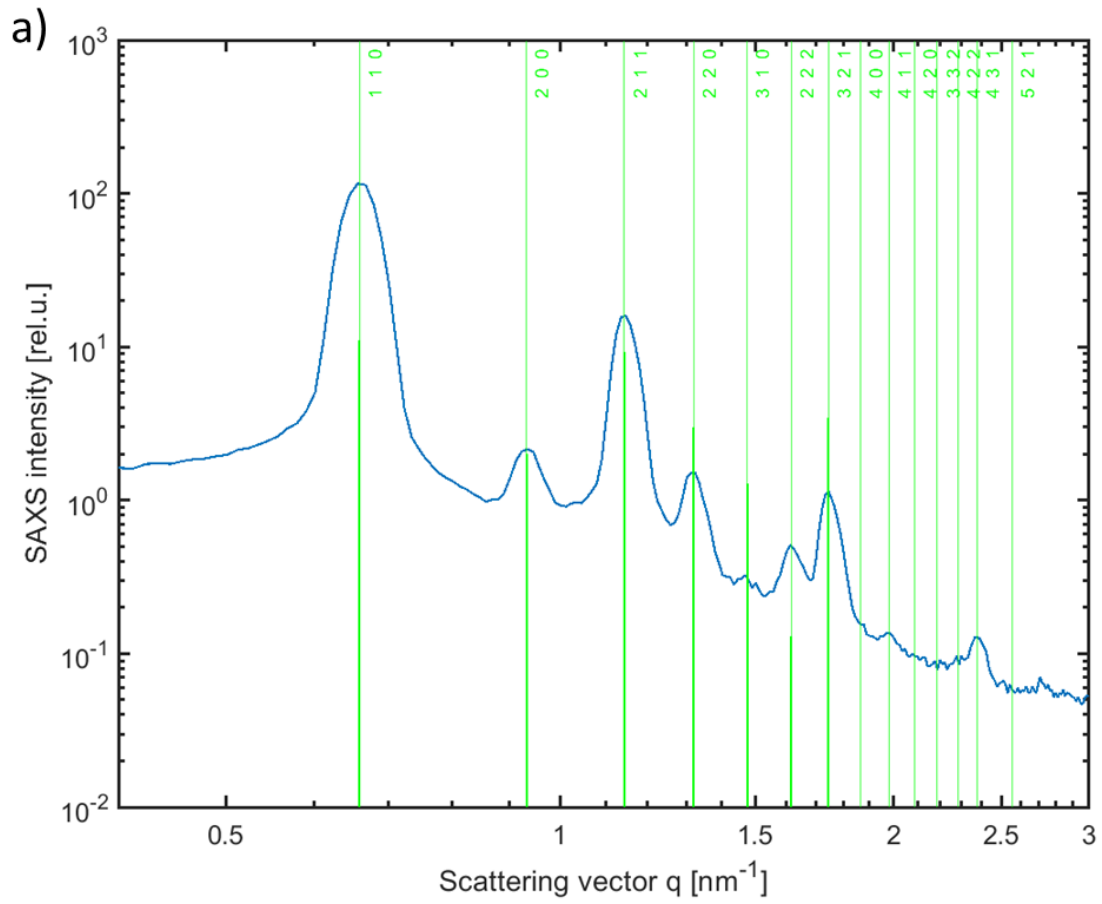
Figure 39: a) Radial SAXS profile at the interface, at 10 hours after the measurement started. Green lines indicate the bcc peaks, thicker lines indicate the theoretical intensities of the peaks, calculated by removal of the form factor of the dispersed NCs and multiplication with the multiplicity factor *m* for the bcc lattice. B) shows the corresponding 2D SAXS pattern.

Right at the interface, we have the highest number of nanoparticles in the whole solution, as the ones from further above slowly diffuse down to form SCs. High numbers of nanoparticles in a high ethanol concentration arrange quickly and randomly. If the particles behaved like hard spheres, e.g. atoms, they would assemble into densest possible structures, fcc or hcp (PD = 0.74), to maximize free volume entropy. But for the case of NCs with soft OA surfaces it has been investigated, that the ligands prefer to uniformly extend around the NC shell. This symmetric arrangement of the OA molecules can exist in the dispersion, but not in a superlattice. As bcc lattice has a more spherically symmetric distribution of voids around a particle, than the fcc lattice, it allows a more uniform ligand shell thickness. This ligand packing frustration might be a key driving force inducing the assembly into a bcc structure [38].

It is also observed that the d-spacings decrease from 10.6 to 9.4 nm over the whole measurement time, which means that the structure densifies (Figure 40). The values slightly fluctuate towards the end of the measurement. From the d-spacings, a reduction of the lattice constant from 14.9 to 13.5 nm and an effective particle diameter D_{soft}, changing from 13 nm to 11.6 nm, were calculated.

By correlating the lattice dimensions with the dimensions of the single NCs, we can discover the arrangement of the particles in the bcc lattice and thus assume, to what extend the ligands are being compressed. Figure 41 shows a schematic representation of the bcc (100) plane at the beginning and at the end of the measurement. At the beginning, particles still maintain a certain distance, the ligands barely touch each other and at the end the particles move closer together. As the bcc structure has the same lattice constant in all directions, the particles get closer together along the long axis of the particle (11.4 nm). As the minimal D_{soft} value is 11.6, there is barely space for ligands between the particles.
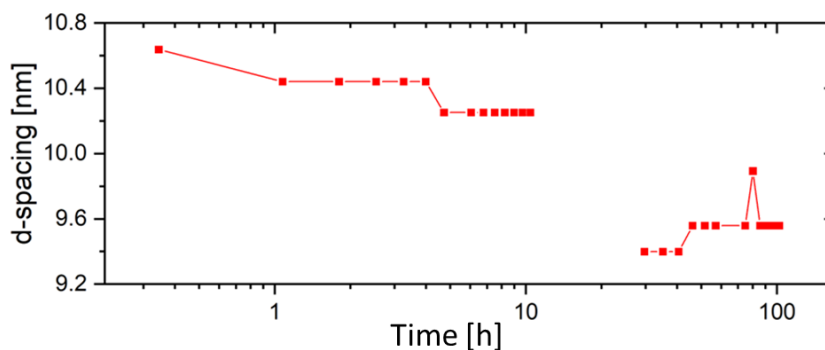

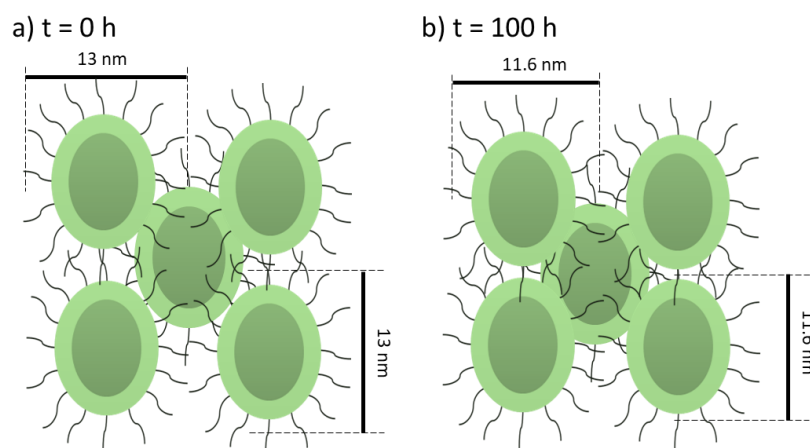Figure 40: d-spacing between the bcc (110) planes over time.

Figure 41: Schematic representation of the bcc (100) plane at a) the beginning (t = 0 h) and b) at the end (t = 100 h) of the measurement at the interface. D_{soft}, the effective particle diameter including ligands, is indicated.

The packing density of the bcc lattice is 68%. The lattice constant of its unit cell is 14.9. So, the volume of the unit cell is 3307.9 nm^3 and the volume of one particle is (if we assume round spheres with a diameter of 10 nm) is 523.6 nm^3. Assuming each OA ligand molecule is 1.8 nm long [14] and the surface of the sphere has an area of 314 nm^2, the ligands occupy a volume of 565.2 nm^3 per particle. A bcc unit cell consists of two particles, so the volume taken up by NCs is 1047.2 nm^3, 2178.1 nm^3 including the ligands. This means that the particles occupy 65.84% of the unit cell, the rest of the void space is occupied by solvent. The lattice contracts to bcc structure with a lattice constant of 13.5 nm and a volume of 2460 nm^3. Now the particles occupy 88.54%, so the ligands now occupy 20.5% of the bcc voids. This explains the high influence of the present solvent on the density of the superlattice. Even in the finished superlattices, 80% of the void space is occupied by solvent.

The SC size fluctuates over time, it tends to grow at the beginning and shrink towards the end of the measurement (Figure 42). The cause for this might be, that with increasing time, single supercrystals grow, but also more supercrystal domains with different sizes are irradiated by the X-ray beam. Thus, the measured crystallite size appears smaller than it might be. Also, the particles and supercrystals are moving around a lot at the interface, and therefore part of the SC which is in the X-ray beam may vary a lot. Crystallite growth therefore couldn't be observed here, but it was possible to estimate an average SC size of 158 nm by using the Williamson Hall plot (Figure 43).
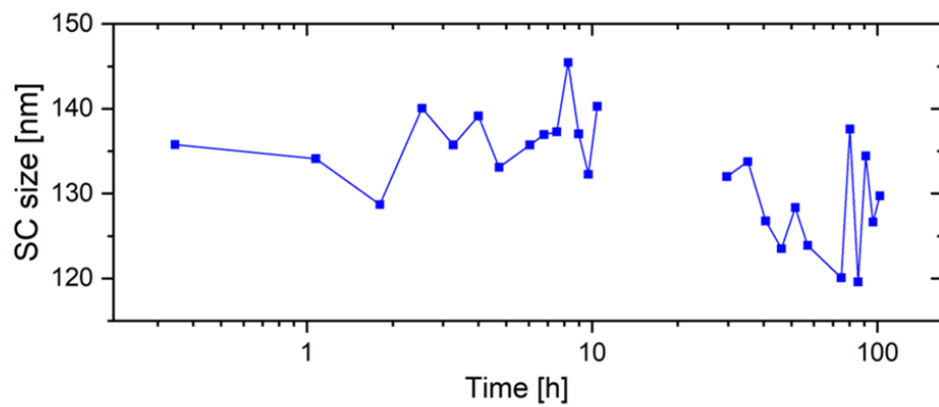
46

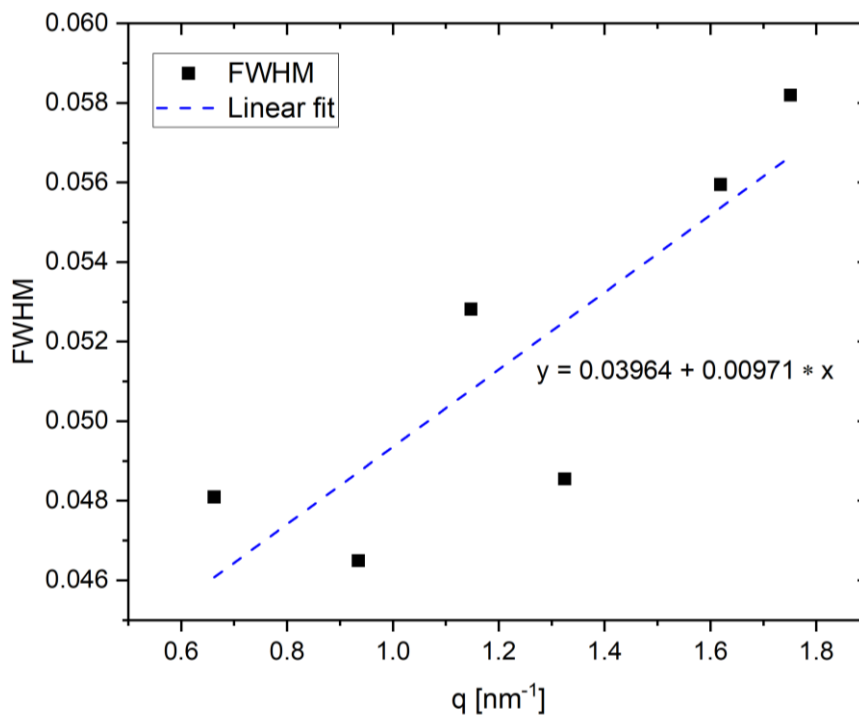Figure 42: Crystallite size (SC size) over time at the interface.

Figure 43: Williamson Hall plot of the SC sizes measured at the interface. The resulting SC size is 158 nm.

5.2.3. Above the interface

From the transmission of the first Position (0 mm), at the beginning of the measurement, the evolution of the concentration of dispersed PbTe/PbS nanoparticles has been calculated and is shown in Figure 44. At the very beginning, the transmission is lower, due to the high number of nanoparticles within the X-ray beam passing through the capillary. It is slowly increasing, as the particles move down do the interface. From the transmission values the initial concentration of NCs was calculated to be 0.2 mg/mL. This is quite realistic, as the solution with the given 5 mg/mL has been diluted before the measurement. At the same position, after about 10 h, SAXS measurements suddenly show peaks, indicating the appearance of a supercrystal (Figure 45). If we compare it to the radial profile at the interface in Figure 39, we see that an additional peak appears in front of the initial bcc (110) peak in and three of the large peaks show a small second hump. Those additional peaks positions comply with the calculated position of the hexagonal-close packed (hcp) structure, with the lattice constants $a = 11$ nm and $c = 22$ nm. The large peaks fit with the bcc structure, but here the lattice spacing of $a = 13.5$ nm, is much smaller than at the interface. The resulting structure at this position is therefore bcc with hcp stacking faults. Q-positions and d-spacings of the different planes in the structures are summarized in Table 11.
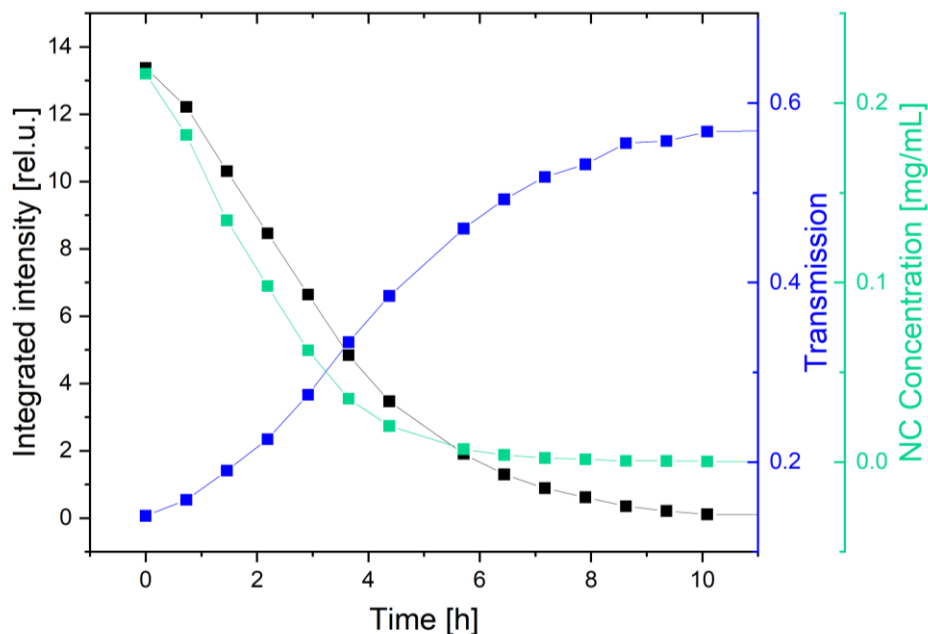

Figure 44: Integrated intensity, transmission, and calculated concentration of dispersed NCs during the first 10 hours of the measurement, at position 1 (0 mm).
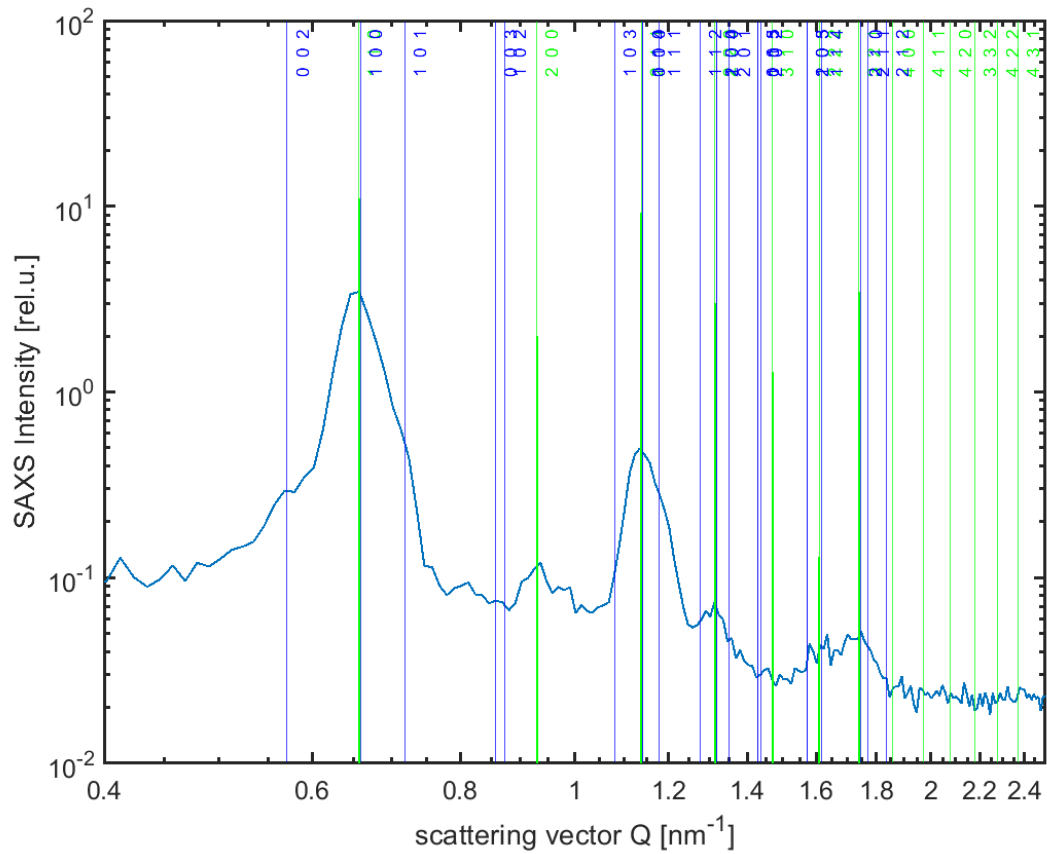
Figure 45: Radial SAXS profile above the interface, blue lines indicate peak positions of the hcp lattice with $a = 11$ nm, $c = 22$ nm; the green lattice indicates the bcc peak positions with: $a = 13.5$ nm.

Table 11: q-positions and corresponding d-spacings of the bcc and hcp planes, obtained from Figure 45.

Peak Nr.	q [nm^{-1}]	d-spacing [nm]	bcc	hcp
1	0.57	11.06		(002)
2	0.66	9.56	(110)	(100)
3	0.70	8.98		(101)
4	0.94	6.72	(200)	
5	1.13	5.56	(211)	(110)
6	1.20	5.24		(111)
7	1.31	4.80	(220)	(200)
8	1.63	3.85	(222)	(114)
9	1.73	3.63	(221)	(210)

In the hcp lattice, the lattice constant a is equal to the diameter D of the particle, including ligands in the case of NCs (Table 1). By subtracting the short diameter of the particle, we get an interparticle distance of 1.8 nm, which is the extra space occupied by the ligands. Assuming round particles, the c-axis would be equal to $c = \frac{4*\sqrt{6}r}{3}$ ($a * 1.633$) which is 17.96 nm. With a radius of 5.7 nm in the c-direction, the c-axis should be 18.62 nm long, it is 22 nm. The resulting interparticle distance of 3.3 nm is approximately the length of the ligands, with 1.7 nm on each side. This means that in the hcp structure, the particles come closer along the shorter diameter (Figure 46).

The hcp and fcc lattices only differ by the sequence of the atomic layers. If we look at the fcc lattice, we can also see a tetragonally distorted bcc lattice. Therefore, we can assume, that due to the higher impact of the different diameters of the particles, the bcc lattice has a longer c-axis and therefore it transforms into a fcc lattice. Additional peaks, i.e. hcp peaks, indicate stacking faults. An example of a 2D SAXS pattern above the interface is shown in Figure 47. Distinct spots are clearly visible, which indicates non-powder like distribution of particles, but rather differently oriented crystals.
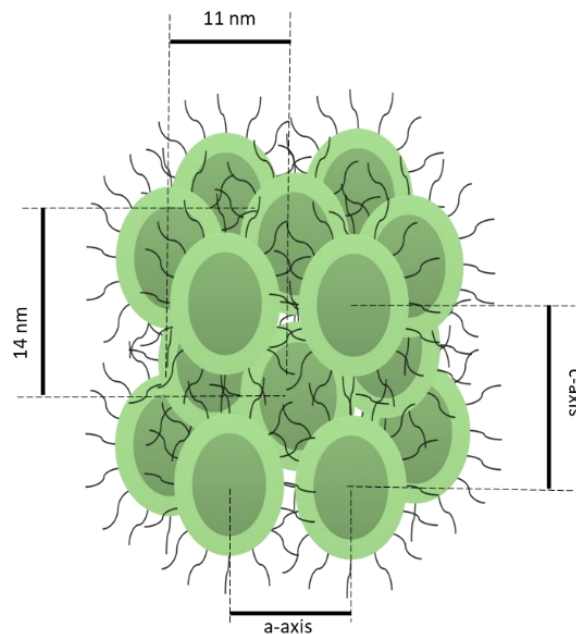

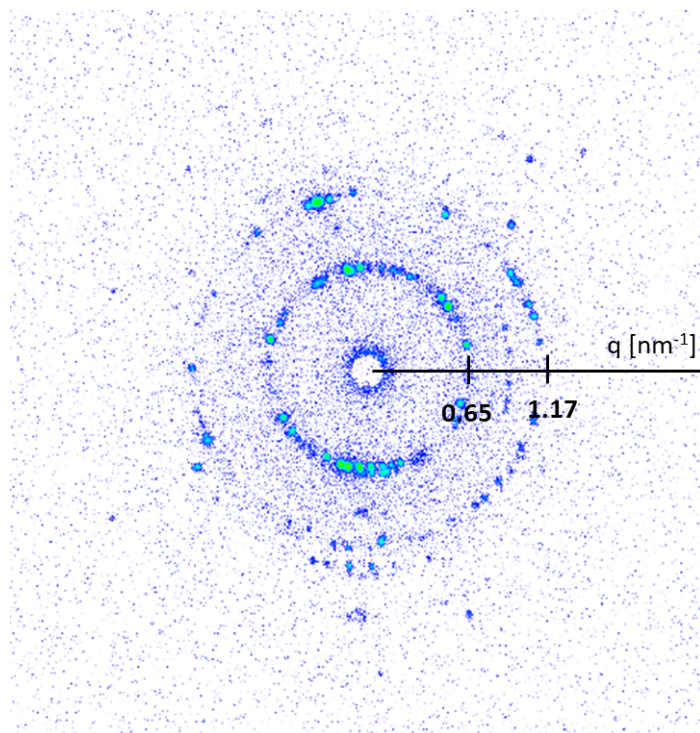Figure 46: Schematic representation of the NCs aligned in an hcp lattice.

Figure 47: 2D SAXS pattern above the interface.

Generally, the softness of the NCs plays a major role in the structure they assemble to. Harder particles, like large NCs with short ligands, act more like atoms and therefore align into close-packed structures, whereas small particles with long ligands tend to assemble into a bcc structure. The softness can be parameterized by the ratio r of the ligand length L to the particle radius R: $r = L/R$. Particles with an $r > 0.7$ interact as soft spheres and tend to form bcc structures, whereas values under 0.7 rather form close packed structures. Based on this model, the investigated NCs with a ratio of ~ 0.4 would be expected to form close-packed fcc or hcp structures [39].

The hexagonal ordering of nanoparticles could also correspond to the [011] projection of the fcc lattice. However, in this projection, the hexagons are stretched by ~15% along the $[0\bar{1}1]$. For hard-sphere colloids it has been predicted, that the fcc structure should be slightly more stable compared to the hcp structure. As traditional models would assume an fcc structure, additional forces must play a role in our case. Because of strong Coulombic, charge-dipole, dipole-dipole interactions, and van der Waals interactions, the behaviour of nanoparticles differs from that predicted for hard spheres. Large dipole moments for nanoparticles with the rock-salt structure have been predicted in previous studies. Such dipole moments may arise from the non-centrosymmetric distribution of polar facets around the nanocrystal. It has also

been investigated that because of the more favourable dipolar coupling in the hcp packing, with odd layers sitting on top of each other, the stability of hcp packing is higher compared to fcc [40,41].

Other studies have demonstrated that, if the concentration of the dispersion is low, nanocrystals tend to assemble into hexagonal lattices, while if it is higher, they rather form a bcc structure. The reason for that is not yet fully understood [42]. A low concentration of particles might mean that the concentration of non-solvent ethanol must be high. Therefore, the particles and especially the ligands interact more with the non-solvent, than with other ligands [39]. A phase transition between hcp and bcc has previously been investigated in heptane and toluol. It is known as the Burgers mechanism and proceeds via the orthorhombic subgroup, which is an intermediate between hcp and bcc (Figure 48) [43,44]. This might explain, why both lattices can be present in the same supercrystal.
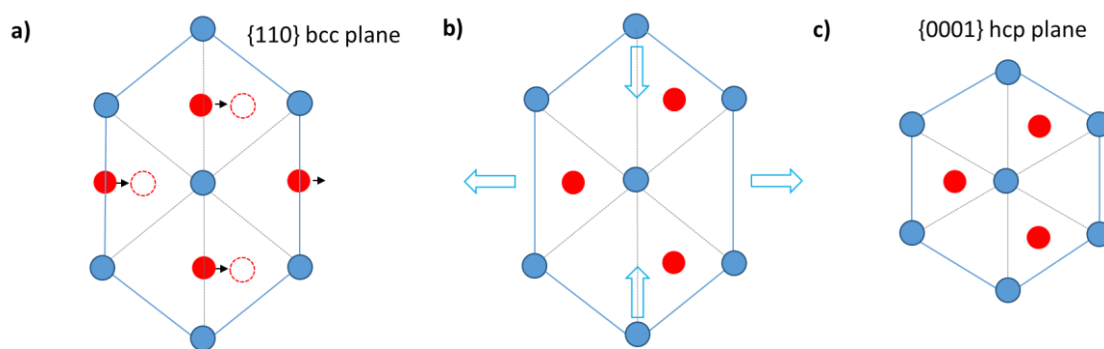

Figure 48: Schematic illustration of the martensitic hcp - bcc transformation.

The hcp and fcc structures are very similar, the only difference between the two is the order of the planes. For this reason, fcc stacking faults are as likely to exist in the bcc SC, as hcp. Bian et.al. previously reported the transition of an fcc superlattice to a final bcc lattice through an intermediate bct-superlattice (Figure 49). This transition is known as the Bain transformation, it is a proof that the bcc and fcc structures are correlated. Studies have shown that the tetragonal distortion only occurs in situations where ligands of neighbouring NCs overlap [39]. In our case, the lattice constant of the initial bcc lattice at Position 1 is smaller than at the interface. Considering the additional peaks that appear at this position, hcp structures with even smaller lattice constants are visible ($a = 11$-12 nm). The additional peaks arise because the shape of the particles plays a higher role, so the d-spacing in different directions are different and the lattice cannot be described by one lattice constant anymore. In smaller particle concentration we observe more ligand-solvent interactions. As shown before, in such a narrow lattice the ligands do overlap [39]. Furthermore, it has previously been investigated, that polycrystalline bcc SCs

exhibit higher conductivity than monocrystalline hcp. This can partly be explained by the shorter nearest-neighbour distance (NND, being a_{hcp} for hcp and $(\sqrt{3}/2) * a_{bcc}$ for bcc) which exponentially increases the hopping probability [5].

If we look at the radial profiles closer to the interface, we can observe the crystallization process *in-situ*, the first peaks are visible after 8-10 hours (Figure 50). For a better visualization of the increasing intensity, the area under the first peak was integrated and is shown vs. time in Figure 51 a. We also observed a shrinking *d*-spacing and SC size, a similar behaviour to that at the interface (Figure 51 b and c). We do not see any double peaks, as we did further above the interface, so the closer we get to the interface, the more homogeneous the bcc structure becomes.
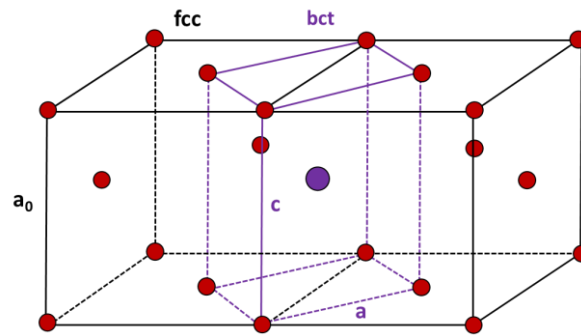

Figure 49: Schematic illustration of the relationship between fcc and bcc over the "intermediate" bct lattice.
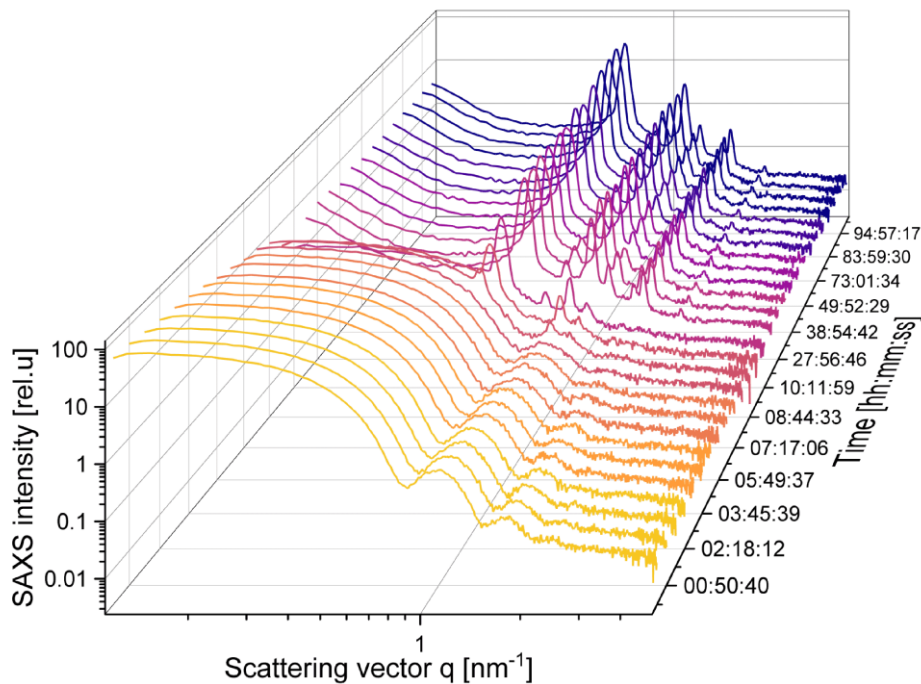

Figure 50: Radial SAXS profiled 3 mm above the interface, over time.
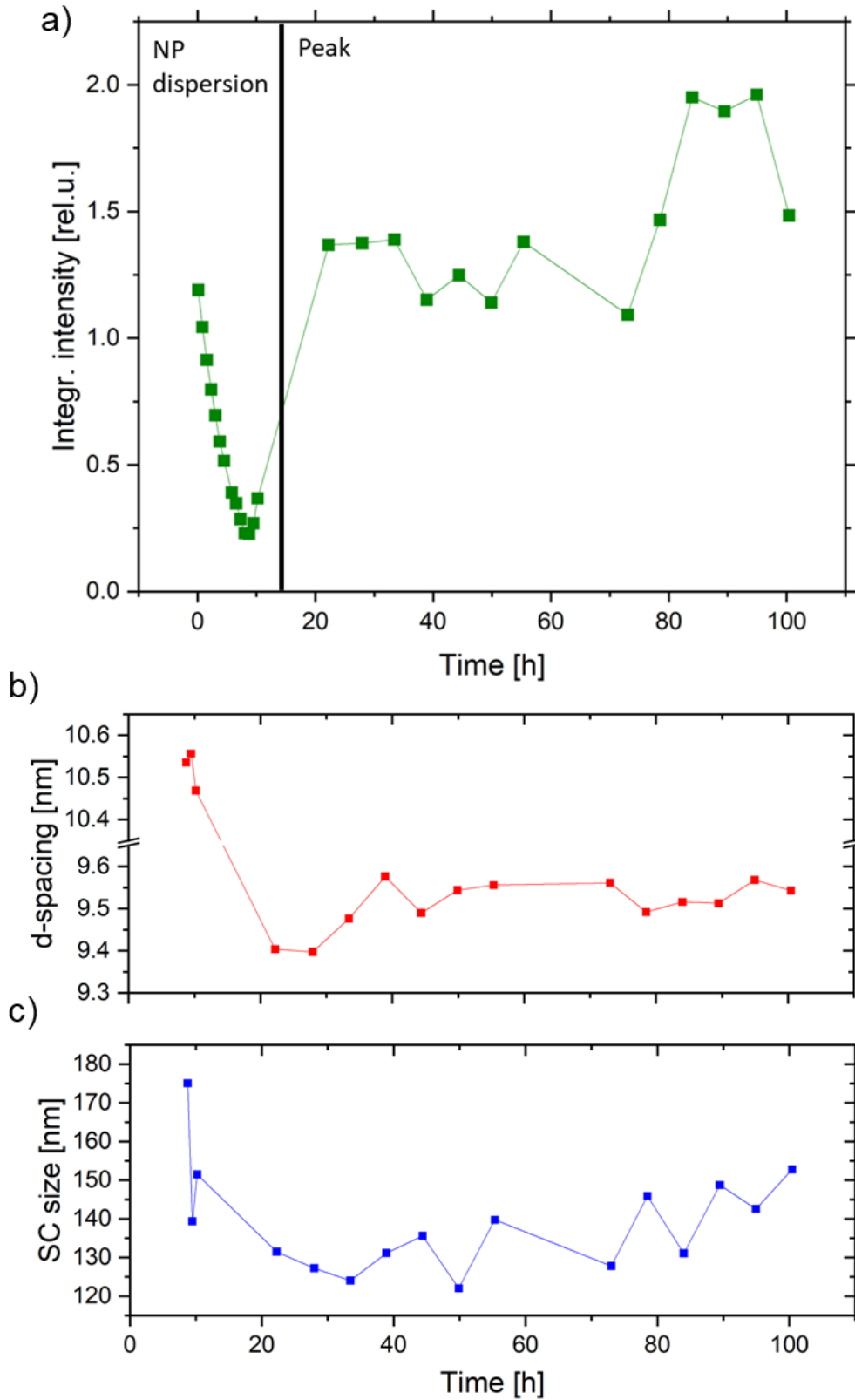
Figure 51: a) Integrated intensity of the first peak. The NC dispersion was integrated from $q = 0.46$ to $q = 0.8$. For the peak, it's the area of the Gaussian fit. b) d-spacing and c) crystallite size over time, 3 mm above the interface.

5.2.4.   Below the interface

At positions below the interface, we also observed highly ordered bcc supercrystals. The diffuse background in the radial SAXS profiles presented in Figure 52 a) is caused by the high amount of ethanol. We do not see a form factor of the dispersed NCs, which indicates that only supercrystals are present here.

The transmission values below the interface are plotted vs. time in Figure 52 b. Comparing the values at up to 10 hours into the measurement, they are higher below the interface than above it (0.32 Figure 52 b vs. 0.25 in Figure 38 a). Due to factors like the changing thickness of the capillary and movements of the sample during the measurements, the measured transmission is slightly lower than we would expect (Glass and Ethanol: 0.43, Table 10). With time, the transmission reaches a value of 0.62, which is close to the calculated value of hexane and ethanol mixed in the capillary. The ring in the 2D SAXS pattern is made of multiple spots, thus confirming the presence of multiple SCs in the beam (Figure 52 b).

In contrast to what we observed at the interface, the *d*-spacings are small at the beginning and become larger towards the end of the measurement (Figure 53 a). The SCs we see here were formed at the interface and slide down along the capillary wall. The SCs are already formed and do not change, therefore we do not observe a change in the *d*-spacings (10.4 nm), only a slight fluctuation at the beginning. Other than during evaporation, the structures here might not be finalized yet. The particles are always moving in the liquid. A slight increase in SC size is observed in Figure 53 b, which might be due to the elimination of stacking faults.

Here, we can clearly see the growth of the SC, from 115 nm to almost 160 nm, clearly visible starting from 50 hours (Figure 53 b). Most probably, we have succeeded to measure the growth of a single SC. This is very likely because here, a smaller number of SCs is present than at the interface, and therefore no other SCs are moving into the X-ray beam during the measurement The crystals that formed at the interface diffused down and agglomerated at the capillary wall.
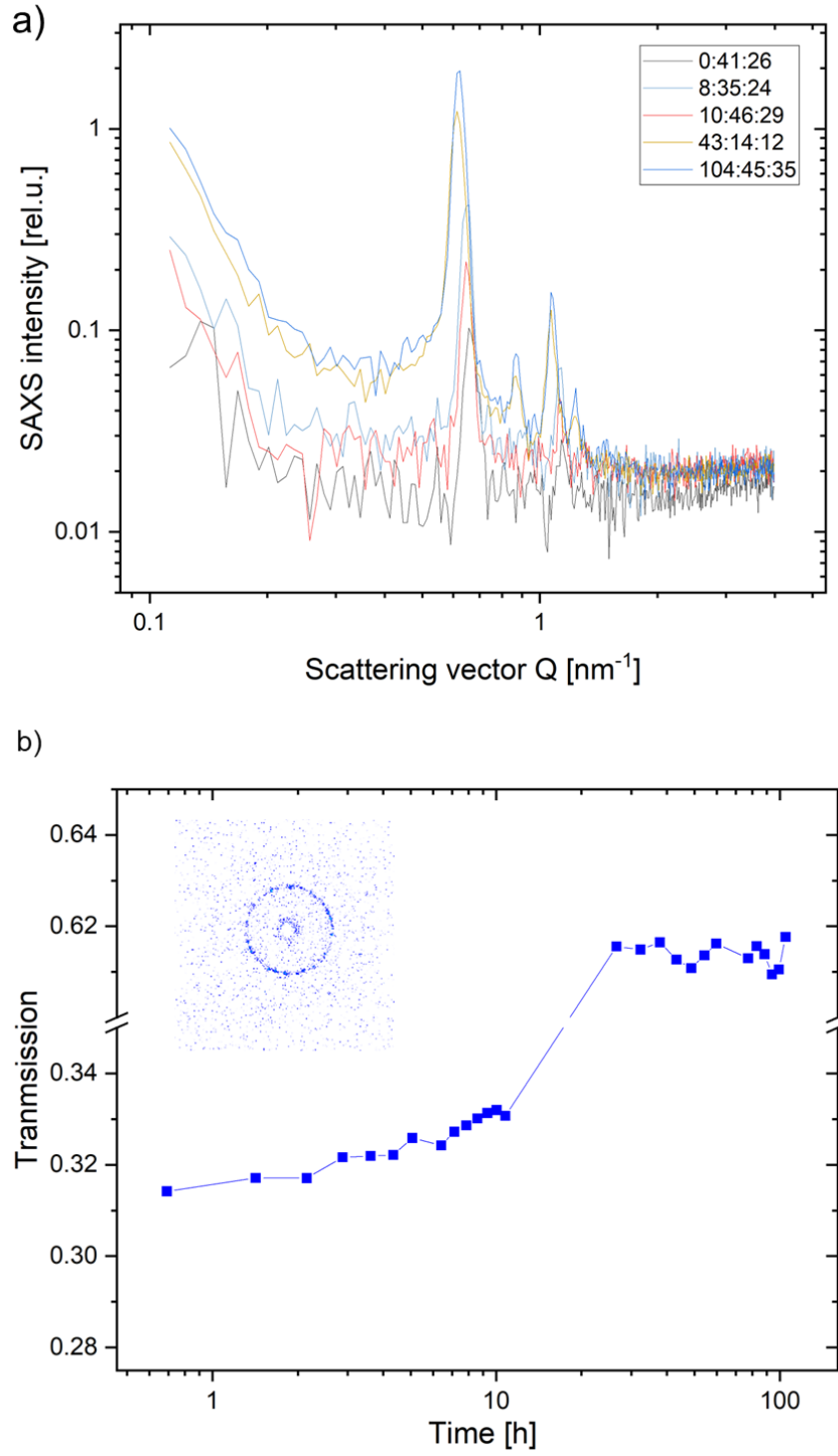
Figure 52: a) Radial SAXS profile and b) transmission with an inset of the 2D scattering pattern, 5 mm below the interface.
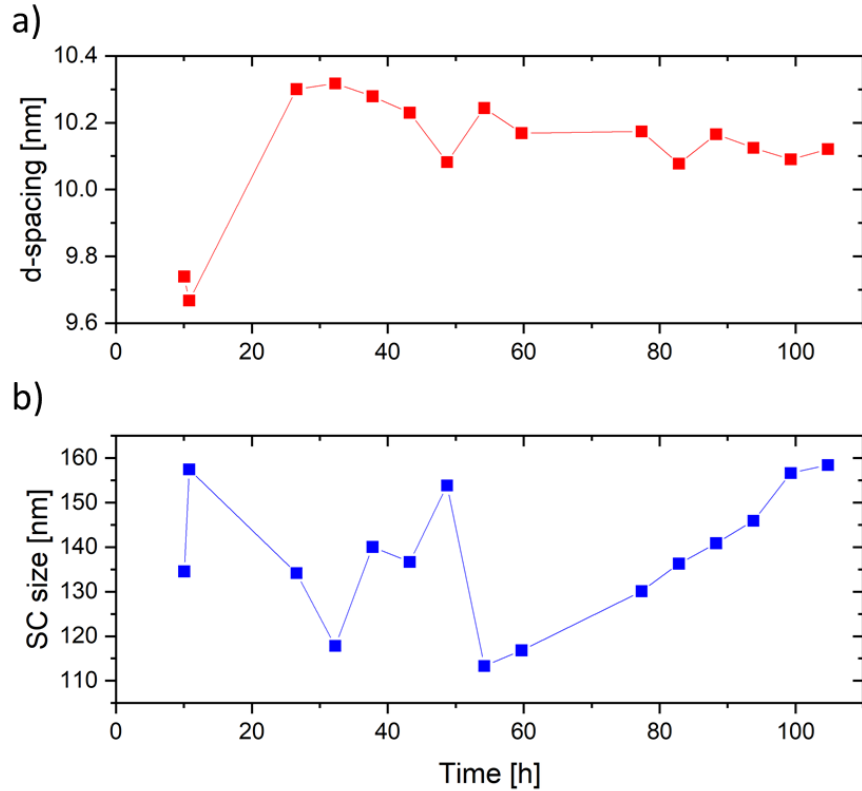
Figure 53: a) *d*-spacing between the (110) planes and b) SC size, 5 mm below the interface.

5.2.5. *Ex-situ* measurements

Two sets of *ex-situ* measurements were performed, the 1st set was 3 weeks after the *in-situ* diffusion experiment and the 2nd one was another three weeks later. During the former measurements, the liquid was still present in the capillary. In contrast to the *in-situ* measurements, almost only the spots of the hcp lattice are visible in the 2D SAXS pattern captured three weeks later (Figure 54). The image was created near the first measured position at 0 mm, where the hcp lattice was also observed *in-situ* (Section 5.2.3.), but rather in form of stacking faults in a mainly body-centred cubic lattice. The angle between the peak position was measured by plotting the integrated intensity along the azimuthal angle *φ* (Figure 54). The angle between hexagonal planes is expected to be 60°, which corresponds to the majority of angles measured [40]. One large peak at 45° is also visible, which may be an indicator for a cubic structure, hidden in the mainly hexagonal lattice.
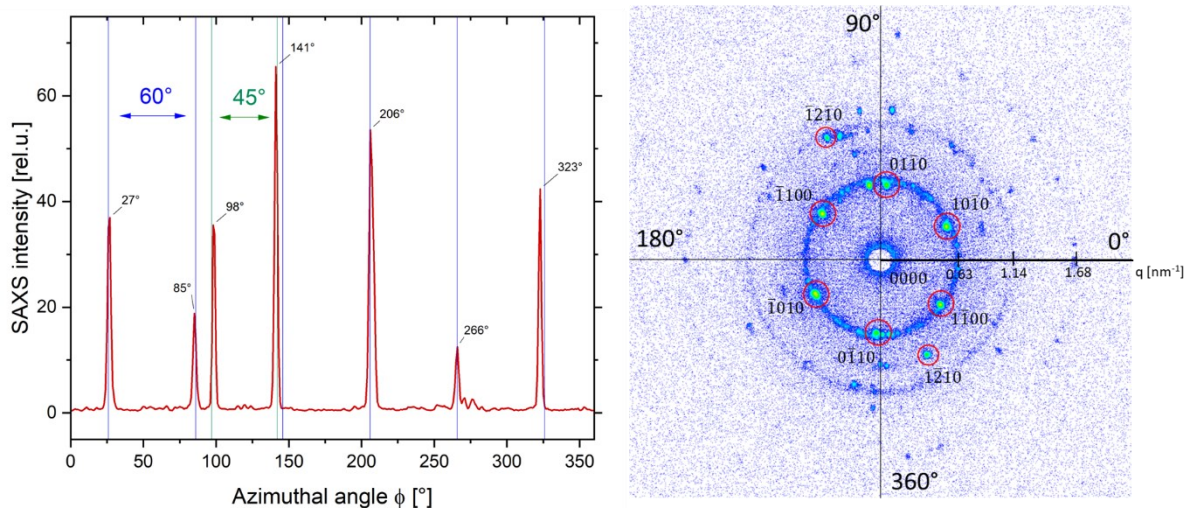
Figure 54: *Ex-situ* SAXS pattern on the right indexed according to the hcp [0000] zone axis, taken near Position 1 (0 mm). The corresponding azimuthal SAXS profile of the first ring is shown on the left.

During the second set of *ex-situ* measurements, the solvent hast already evaporated (Figure 55). To find the locations with a high number of particles, a quick scan over the whole area was performed first (Figure 56). Then, a few 2D patterns at an exposure time of 1000 seconds were collected. From those, one scattering profile with distinct peaks was picked out and is shown in Figure 57. Its azimuthal profile reveals an angle of 35° between the peaks (Figure 57).

Figure 55: Photography of the capillary, as the liquid evaporated.

Figure 56: 2D scan over the whole capillary, 0.5 s/measurement.

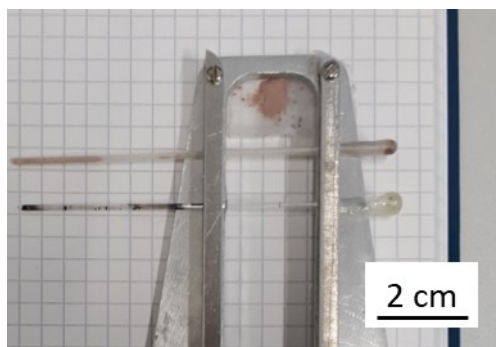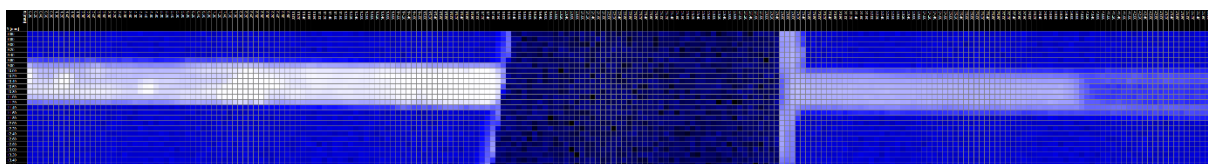Assuming two crystals with 70° spacing between the spots of the reciparocal lattice, we assume that two distorted hcp lattices were measured at this position. The measured angles are not the typical angles of the hcp lattice, so our supercrystals may have their own individual shape. The shapes measured with SAXS may correlate with the shapes visible in the microscope (Figure 60), as the angle of 70° appears in both images.

The supercrystal sizes form both 2D patterns were calculated form the standard deviation of the single spots and are summarized in Table 12. The values obtained by this method are larger and more accurate than the one from the radial profiles. The reason for that is that previously, we measured the width of the peak that covers all smaller spots, which is clearly wider that a single spot. The peaks also seem larger when measured on the N8, because the diameter of the beam is 500 μm, while it is 300 μm on the NanoStar. The divergence from the primary beam is therefore larger on the N8, resulting in wider peaks.
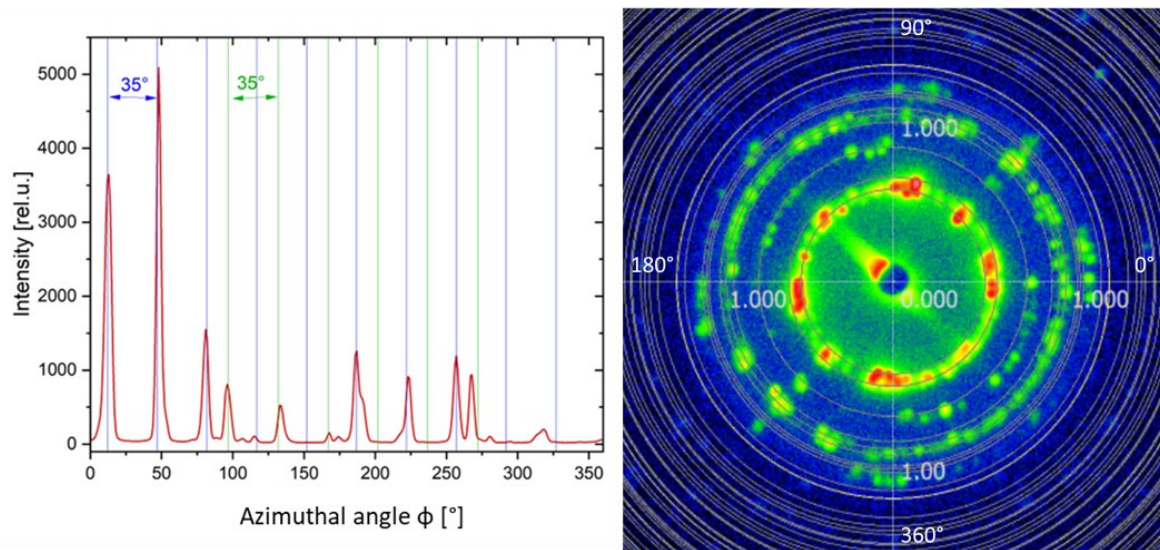
Figure 57: *Ex-situ* SAXS pattern as the liquid evaporated (exposure time 1000 sec) on the right, at $x = 7.2$ mm and $y = 11$ mm. Peak positions of the hcp lattice with $a = 13.5$ and $c = 22$ nm, are indicated. The corresponding azimuthal SAXS profile of the first ring is shown on the left.

A majority of the particles crystallize into a bcc structure during the *in-situ* diffusion process. Afterwards, they tend to reassemble into the denser hexagonal structure (*PD* hcp > *PD* bcc (Table 1)). Pattern 1 (Figure 54) even shows an almost single hexagonal crystal, with a mean size of 363.2 ± 47.6 nm. It is likely that the distinct spots of the *ex-situ* patterns represent the supercrystals which are visible in the LIMI. With this assumption, one can estimate that the ~ 20 x 20 μm sized crystals visible in Figure 60 b and c are made of about three ~ 363 x 363 nm sized single domains.

Table 12: Supercrystal sizes, calculated from the standard deviations obtained from the 2D SAXS patterns.

	Pattern 1 (Figure 54)			Pattern 2 (Figure 57)	
σ	FWHM	SC size [nm]	σ	FWHM	SC size [nm]
0.0165	0.0194	323.9	0.0094	0.0110	569.7
0.0153	0.0180	348.7	0.0103	0.0122	517.1
0.0143	0.0168	374	0.0100	0.0118	534.7
0.0175	0.0206	305.8	0.0087	0.0102	615.7
0.0147	0.0173	363.7	0.0097	0.0114	550.7
0.0163	0.0192	327.6	0.0093	0.0109	573.9
0.0165	0.0194	323.5	0.0087	0.0102	615.9
0.0151	0.0178	354			
0.0119	0.0140	449.8			
0.0147	0.0173	363.9			
0.0116	0.0137	460.1			
Mean		363.2 ± 48			568.2 ± 35

After the *ex-situ* measurements, microscopy images of the capillary were taken (Figure 58). Parallelepipeds of two sizes: ~2 x 2 µm (Figure 58 a) and ~20 x 20 µm (Figure 58 c), as well as aggregated particles (Figure 58 b), can be seen there. The small crystals cover almost the whole glass wall, whereas the large ones are only visible in the bottom part, stretching along the capillary like thin ribbons. Unfortunately, we only measured a small area of the capillary *in-situ*: around the initial interface. Therefore, the self-assembly process of the large supercrystals remains unknown.

It is remarkable, that if we look at the image of the capillary, we see that transparent liquid is present above the darker area with particles sticking to the capillary wall. This means that all the NCs diffused downwards. We see that many particles have fallen to the bottom of the capillary. The angles are in the range from 56° x 124° to 70° x 110°. From these measurements, we tried to estimate the inner structure of the crystals. Some have a perfectly rhombohedral shape (Figure 59 a and c), a form which can also be seen in the two-dimensional hexagonal lattice (Figure 60). Others, shaped more like parallelograms, might have a rather cubic inner structure (Figure 59 b).
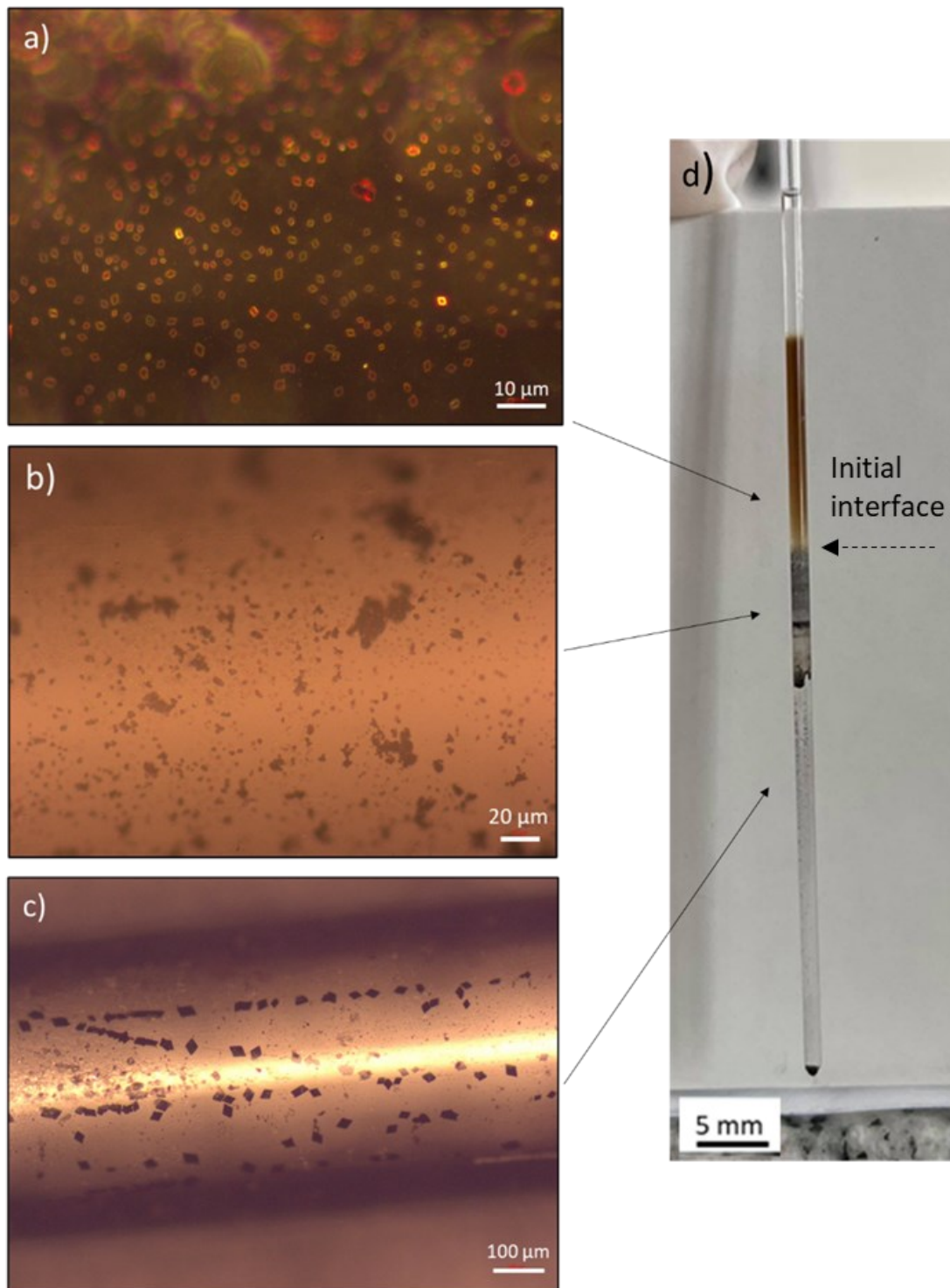
Figure 58: Overview over the microscopy images taken at the shown locations on the capillary. In a) small crystals can be seen, which are present on nearly the whole capillary (image taken in dark mode). In b) aggregated particles can be seen, which are present at the lower part of the capillary, below the initial interface. In c) large SCs are visible, which also appear at the lower part of the capillary.
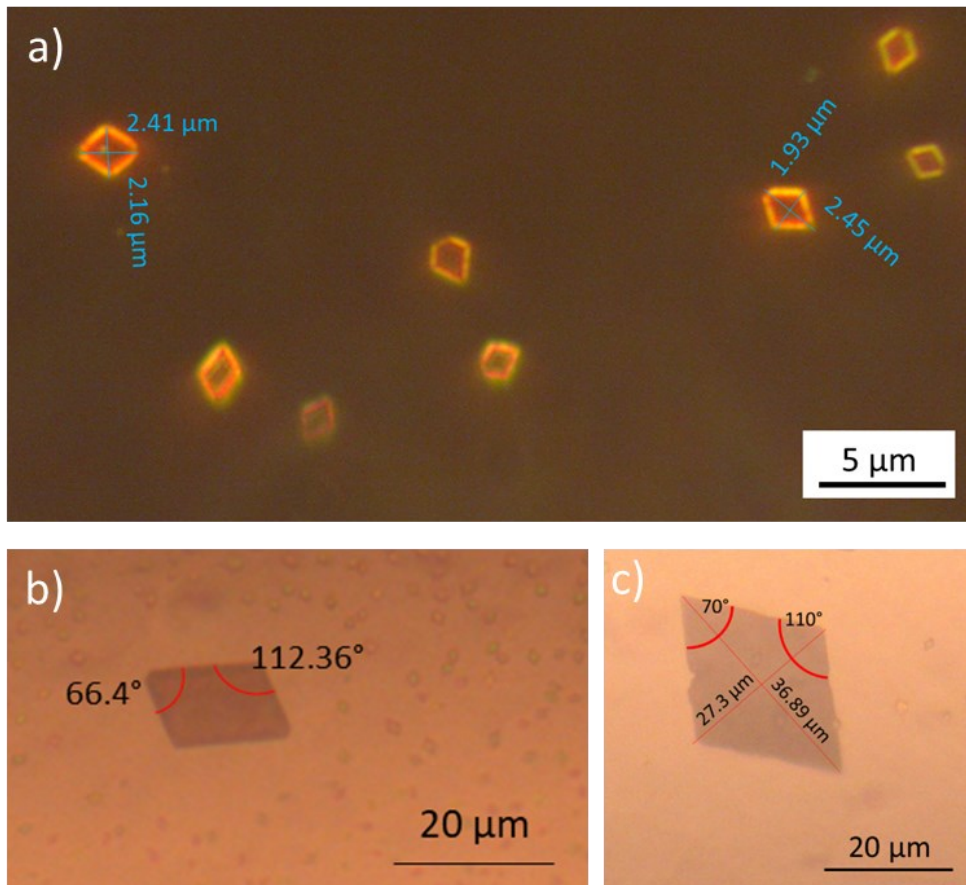
Figure 59: Microscopy images. a) 200x magnification, dark mode, b) Larger SC, 50x magnification and c) rhombohedral SC, 50x magnification.

Figure 60: Schematic illustration of the rhombohedral cell inside the hexagonal lattice.

5.3. Summary

From the XRD measurements, we detected the fcc crystal structures of PbTe and PbS. Moreover, we were able to observe that the particles are not perfectly spherical, but rather have certain facets. We could see that after evaporation of the solvent hexane, the NCs assembled in layers, aligned along those facets. We also found out that if the number of particles on the substrate is lower, the crystallinity of the structures ten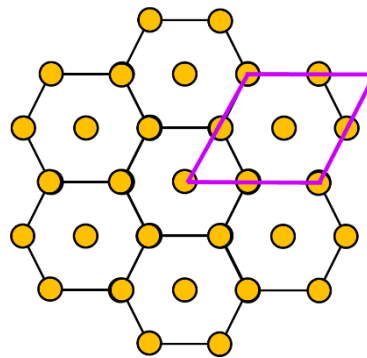ds to become higher. Although accurate particle dimensions were obtained with XRD, no indication of an asymmetrical shape could be observed. The shape of the single NCs was previously determined form radial SAXS profiles of dispersed particles [36]. These dimensions were employed in this work and are summarized in Table 13. and illustrated in Figure 61. The structure the particles assembled to was mainly bcc, because here the ligands can arrange spherically around the NC. The bcc structures obtained through evaporation and diffusion hihgly differ from one another. During the evaporation experiments, we achieved a very dense crystal lattice, because the solvent evaporated quickly and only the dry NCs remained on the substrate. In contrast to that, the liquids are present in the capillary during the whole *in-situ* diffusion experiment. They are filling the voids between the particles, thus keeping them furhter apart. We also found the existence of hcp stacking faults, the two lattices can coexist as they are related through the Burgers mechanism. When the concentration of non-solvent is high, a hcp structure can form due to the interaction of the ligands with the non-solvent, resulting in denser structures than bcc. At the initital hexane-ethanol interface, the highest number of NCs is present. The bcc superstructures that formed here become denser with time. Some of the SCs that form at the interface between hexane and ethanol slide down, but their size may still change because the particles are moving in the liquid and stacking faults are being eliminated.

An overview over the obtained lattice parameters in the diffusion experiment is shown in Table 14 and Table 15. After correlating those parameters with the dimensions of the NCs, a schematic representation of the NCs aligned in the two lattices present, bcc and hcp, was made (Figure 62).

Table 13: Dimensions of the particle.

Short axis [nm]	9.2
Long axis [nm]	11.4
Ligand length [nm]	1.8
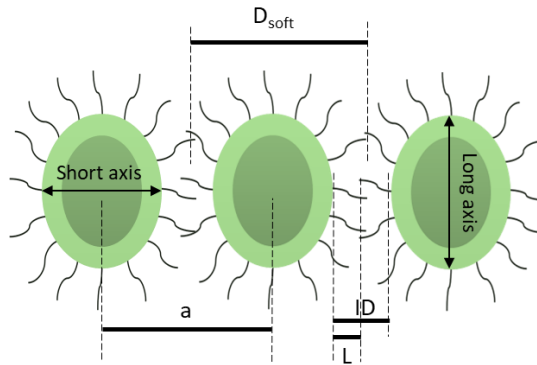
Figure 61: Schematic illustration of the core shell particles, with *a* as the lattice constant, D_{soft} as the effective particle diameter (excluding overlapping ligands), *ID* as interparticle distance, and *L* as ligand length (excluding overlapping ligands).

Table 14: Lattice parameters along the short axis (9.2 nm).

	Position [mm]	D_{soft} [nm]	*ID* [nm]	*L* [nm]	*a* [nm]	
	0	11	1.8	0.9	11	hcp
Above IF	4.5	12.7	3.5	1.8	14.7	
	5	11.9	2.7	1.3	13.7	
IF	5.75	11.6	2.4	1.2	13.4	bcc
Below IF	6.25	12.4	3.2	1.6	14.3	
	11.75	12.4	3.2	1.6	14.3	

Table 15: Lattice parameters along the long axis (11.4 nm).

	Position [mm]	D_{soft} [nm]	ID [nm]	L [nm]	a [nm]	
	0	14.7	3.3	1.7	22*	hcp
Above IF	4.5	12.7	1.3	0.7	14.7	
	5	11.7	0.5	0.2	13.7	
IF	5.75	11.6	0.2	0.1	13.4	bcc
Below IF	6.25	12.4	1.0	0.5	14.3	
	11.75	12.4	1.0	0.5	14.3	

*c axis in hcp
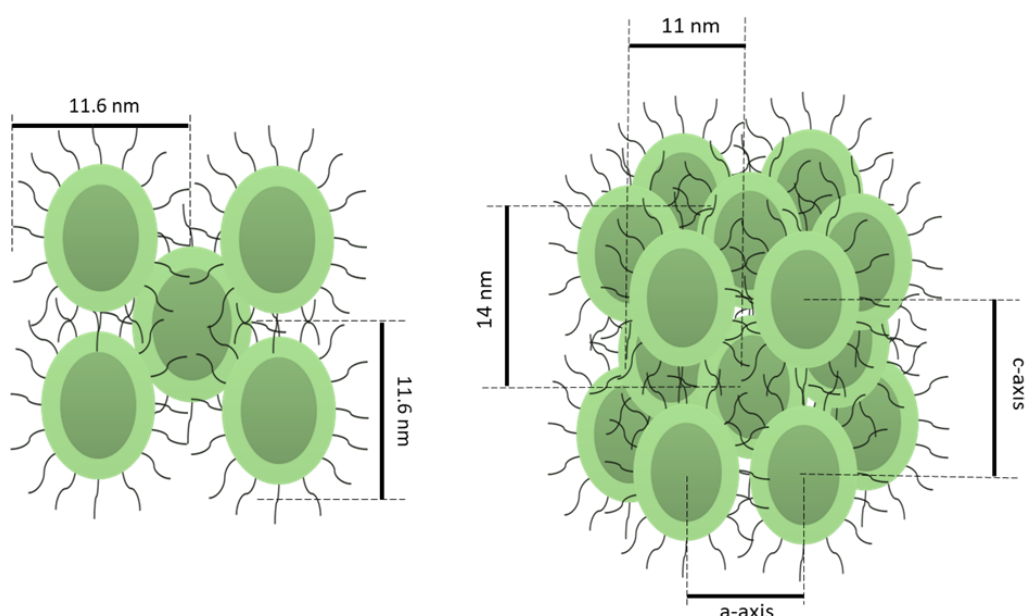
Figure 62: Schematic representation of the NCs aligned a) in the bcc structure at the interface b) in the denser hcp structure above the interface.

In the supercrystal, the interparticle distance is the smallest along the long axis at the interface (0.2 nm). This means that here shells of the particles nearly touch. At this position, the high amount of dispersed particles and non-solvent possibly caused them to arrage closely toghether. Further above and below the interface, the the superstructures are broader. Above the interface, the interparticle distance ID along the long axis is as large, as the length of two ligands opposite from eachother (3.3 nm). Along the short axis it is exactly 1.8 nm, which is one ligand length. This means that we were able to correlate the particle dimensions with the resulting superstructures, taking the ligand dimensions into account.

After weeks and even months passed, the liquid slowly evaporated and dry SCs remained in the capillary. With this process, were able to achieve almost monocrystalline superlattices. The bcc-hcp structures assembled to nearly pure hcp SCs. A reason for that might be the evaporation of the solvent, that causes the NCs to rearrange into a denser structure.

SC sizes achieved through evaporation of the solvent are very small (40 nm), while they grow to up to 140 nm during the *in-situ* diffusion experiment (Table 16). It is remarkable, that the SCs still become a lot larger after weeks and months after the *in-situ* diffusion experiment.

The radial SAXS profiles obtained from the different experiments are compared (Figure 63). Here, the similar spacings between the peak positions indicate similar crystal structures, but crystal dimensions are clearly different, which can be seen from the varying peak positions. The overall intensity of the radial SAXS curve obtained from the evaporation experiment is much higher than the other ones. A reason for that difference in intensities is, that the evaporation experiment was carried out at the N8 with a beam diameter of 500 μm, while the beam at the NanoStar, where we observed the diffusion process, is 300 μm.

The intensities, so the numbers of measured particles during the *in-situ* diffusion experiment are highest at the interface and lowest below the interface. Due to the high concentration of non-solvent ethanol and the resulting attractive forces between particles at the initial interface, most dispersed NCs accumulate there. Supercrystallization takes place here, and the SCs which slide down along the walls of the capillary are measured below the interface.

Table 16: Overview over obtained features of the structures that resulted in the different assembly-mechanisms.

Mechanism	D [nm]	Sample region	Crystal structure	a (x c) [nm]	SC size [nm]
Evaporation	6 ± 0.9		bcc	8	41 ± 4
Diffusion *in-situ*	11.4 x 9.2	above IF	bcc and hcp	13 (11 x 22 for hcp)	139 ± 13
		IF	bcc	14.9 to 13.5	132 ± 7
		below IF	bcc	13.7 to 14.3	138 ± 14
Diffusion *ex-situ*	11.4 x 9.2	above IF	hcp	13.5 x 22	433 ±109
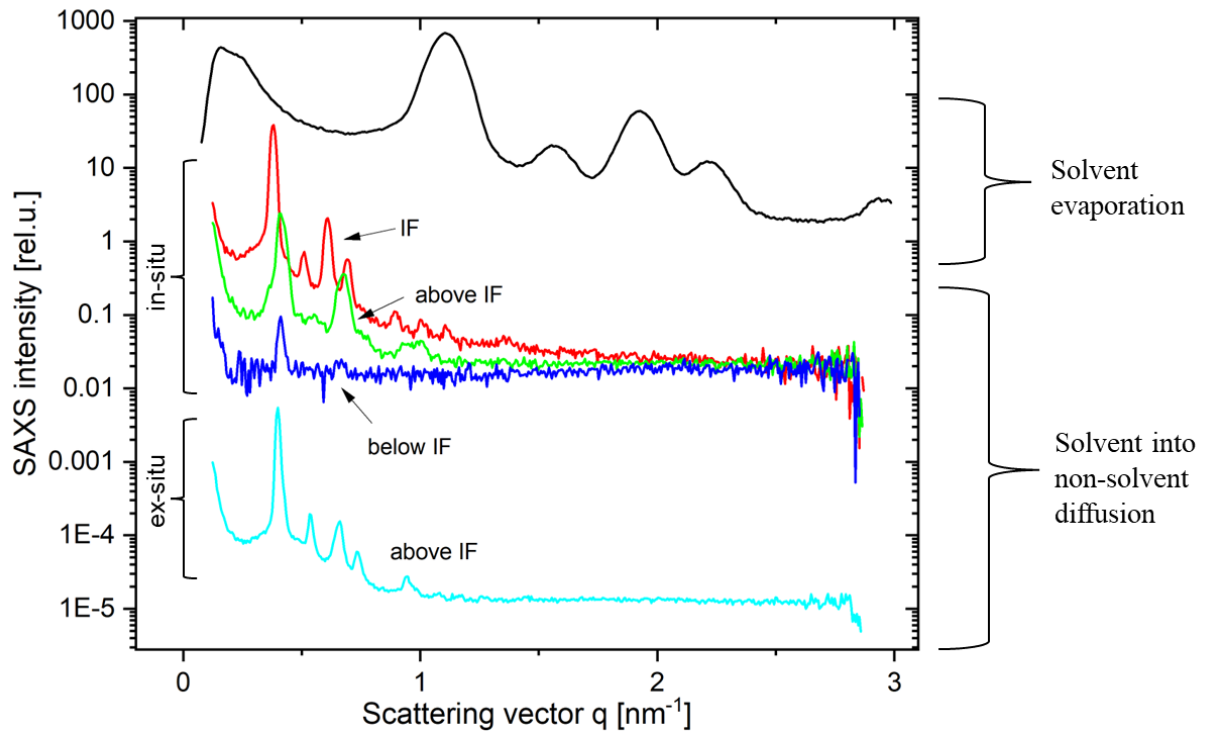
Figure 63: Overview over obtained radial SAXS profiles in the different experiments. The upper black line was obtained at Position 17 on the sample with the evaporated solvent, The three middle ones were obtained from the diffusion experiment, one at the interface (IF), one above and one below. The lowest curve is a radial integration of one of the *ex-situ* SAXS patterns.

The lowest intensitiy was measured *ex-situ*. Here, no liquid and therefore no dispersed particles are present. Those measurements revealed that after the *in-situ* measurements, our SCs rearranged into rather hexagonal, and nearly monocrystalline, lattices. The microscopy images show large crystallites, which have similar angles as the ones measured in SAXS.

6. Conclusion and Outlook

All in all, we achieved larger and more ordered supercrystals in the diffusion experiment than during evaporation of the solvent. This is because the diffusion of a non-solvent into a solvent is a more controlled process and crystallization happens a lot slower. Nevertheless, the structures obtained by evaporation are much denser because the solvent fully evaporates, and the particles can align as close as possible. In contrast to that, NCs in the capillary are being kept further apart during the whole process due to the presence of the non-solvent ethanol.

As many processes and mechanisms play a role during the self-assembly processes, we do not know exactly what causes the particles to arrange in such structures. From similar experiments discussed in literature, we were able to make a few assumptions which may apply to our particles and assembly conditions. The amount of information we gained from only one experiment: diffusion of a non-solvent into the NC dispersion, is fascinating to me. We correlated the transmission with the concentration of a certain substance in the capillary and compared the concentrations with the SAXS patterns. We were able to closely investigate supercrystal growth *in-situ* and even to grow supercrystals visible with the naked eye. This method may be more complicated and time-consuming, than the evaporation method, but the results are astonishing. This thesis demonstrates how many different, complex self-assembly mechanisms can take place in such a small space as a capillary.

After finishing the *in-situ* measurements, I left the capillary in the SAXS instrument. Busy with the data evaluation, I haven't taken the time to take the capillary out for a few weeks. As we saw later under the microscope, this was a true blessing for the supercrystals. They arranged to nearly perfect, hexagonal single crystals. Therefore, this work may provide a step forward in the field of the development of functional nanocomposites, where large and monocrystalline superlattices are desired. An ordered arrangement of NCs may enhance the properties of the single NCs.

Nevertheless, many questions remain unanswered: why do the supercrystals grow in such thin lines and perfect shapes? What exactly influences the structure the NCs assemble to? Which crystal lattice is favourable for production, as well as for the efficiency of the nanostructured device they are to be used in? To find answers to these questions, it is no big effort to reproduce this experiment. What is clearly needed though, is patience. As they saying goes, good things come to those who wait.

7. References

[1]   D. Wu, X. Tong, L. Zhao, and W. Li, "Superior Thermoelectric Performance in PbTe-PbS Pseudo-binary : Extremely Energy & Environmental Science Superior thermoelectric performance in PbTe – PbS pseudo-binary : extremely low thermal conductivity," *Energy Environ. Sci.*, May, 2015.

[2]   Helmut Cölfen and Markus Antonietti, *Mesocrystals and Nonclassical Crystallization*. 2008.

[3]   M. Ibáñez *et al.*, "Core-shell nanoparticles as building blocks for the bottom-up production of functional nanocomposites: PbTe-PbS thermoelectric properties," *ACS Nano*, vol. 7, no. 3, pp. 2573–2586, 2013.

[4]   R. Mulla and C. W. Dunnill, "Core-shell nanostructures for better thermoelectrics." p. 17, 2021.

[5]   A. Maier *et al.*, "Structure–Transport Correlation Reveals Anisotropic Charge Transport in Coupled PbS Nanocrystal Superlattices," *Adv. Mater.*, vol. 32, no. 36, Sep. 2020.

[6]   Y. I. Ravich, B. A. Efimova, and I. A. Smirnov, *Semiconducting Lead Chalcogenides*. 1970.

[7]   M. V Kovalenko *et al.*, "Prospects of Nanoscience with Nanocrystals," *ACS Nano*, 2014.

[8]   R. Miranti *et al.*, "Exclusive Electron Transport in Core@Shell PbTe@PbS Colloidal Semiconductor Nanocrystal Assemblies," *ACS Nano*, vol. 14, no. 3, pp. 3242–3250, 2020.

[9]   M. V. Kovalenko, "Opportunities and challenges for quantum dot photovoltaics," *Nat. Nanotechnol.*, vol. 10, no. 12, pp. 994–997, 2015.

[10]   R. Miranti *et al.*, "Electron transport in iodide-capped core@shell PbTe@PbS colloidal nanocrystal solids," *Appl. Phys. Lett.*, vol. 117, no. 17, 2020.

[11]   M. J. Speirs *et al.*, "Origin of the increased open circuit voltage in PbS-CdS core-shell quantum dot solar cells," *J. Mater. Chem. A*, vol. 3, no. 4, pp. 1450–1457, 2015.

[12] J. Van Embden, A. J. Jasieniak, A. D. E. Gómez, and A. P. Mulvaney, "Review of the Synthetic Chemistry Involved in the Production of Core / Shell Semiconductor Nanocrystals," pp. 457–471, 2007.

[13] M. A. Boles, D. Ling, T. Hyeon, and D. V Talapin, "The surface science of nanocrystals," *Nat. Mater.*, vol. 15, pp. 141–154, 2016.

[14] A. Reichhelm, D. Haubold, and A. Eychmüller, "Ligand Versatility in Supercrystal Formation," vol. 1700361, pp. 1–17, 2017.

[15] M. A. Boles, M. Engel, and D. V. Talapin, "Self-assembly of colloidal nanocrystals: From intricate structures to functional materials," *Chem. Rev.*, vol. 116, no. 18, pp. 11220–11289, 2016.

[16] S. Sacanna and D. J. Pine, "Current Opinion in Colloid & Interface Science Shape-anisotropic colloids : Building blocks for complex assemblies," *Curr. Opin. Colloid Interface Sci.*, vol. 16, no. 2, pp. 96–105, 2011.

[17] C. Wang, C. Siu, J. Zhang, and J. Fang, "Understanding the forces acting in self-assembly and the implications for constructing three-dimensional (3D) supercrystals," vol. 8, no. 8, pp. 2445–2466, 2015.

[18] Z. Fan and M. Grünwald, "Orientational Order in Self-Assembled Nanocrystal Superlattices," *J. Am. Chem. Soc.*, vol. 141, no. 5, pp. 1980–1988, Feb. 2019.

[19] M. Burian *et al.*, "A Shape-Induced Orientation Phase within 3D Nanocrystal Solids," *Adv. Mater.*, vol. 30, no. 32, 2018.

[20] V. K. Pecharsky and P. Y. Zavalij, *Fundamentals of Powder Diffraction and Structural Characterizarion of Materials*, Second Edi. Springer, 2009.

[21] Emil Zolotoyabko, *Basic Concepts of Crystallography*. 2011.

[22] Y. Waseda, E. Matsubara, and K. Shinoda, *X-Ray Diffraction Crystallography*, vol. 46, no. 1. 2016.

[23] P. Bandyopadhyay and C. U. Segre, "Mucal Periodic Table." http://www.csrri.iit.edu/mucal.html.

[24] B. D. Cullity and S. R. Stock, *Elements of X-Ray diffraction*, Third Edit., vol. 108, no. 2. Pearson, 1979.

[25]   H. Schnablegger and Y. Singh, *The SAXS Guide*, 4th ed. Anton Paar, 2017.

[26]   G. Popovski, "MULIP SAXS-2D ver. 2019.10.18." 2019.

[27]   B. L. Henke, E. M. Gullikson, and J. C. Davis, "X-ray interactions: Photoabsorption, scattering, transmission, and reflection at E = 50-30, 000 eV, Z = 1-92," *Atomic Data and Nuclear Data Tables*, vol. 54, no. 2. pp. 181–342, 1993.

[28]   O. Paris, "Small-Angle Scattering (SAXS): Principles and Selected Applications Outline," 2005.

[29]   S. A. Speakman, "Estimating Crystallite Size using XRD," *MIT Cent. Mater. Sci. Eng.*

[30]   "MATLAB ver. R2020b." The Mathworks, Inc., Natick, Massachusetts, 2020.

[31]   M. Wojdyr, "Fityk: A general-purpose peak fitting program," *J. Appl. Crystallogr.*, vol. 43, no. 5 PART 1, pp. 1126–1128, 2010.

[32]   M. Burian, G. Fritz-Popovski, M. He, M. V. Kovalenko, O. Paris, and R. T. Lechner, "Considerations on the model-free shape retrieval of inorganic nanocrystals from small-angle scattering data," *J. Appl. Crystallogr.*, vol. 48, no. July, pp. 857–868, 2015.

[33]   A. A. Azab, A. A. Ward, G. M. Mahmoud, E. M. El-Hanafy, H. El-Zahed, and F. S. Terra, "Structural and dielectric properties of prepared PbS and PbTe nanomaterials," *J. Semicond.*, vol. 39, no. 12, pp. 1–8, 2018.

[34]   Phenomenex, "Solvent miscibility table," *Phenomenex Cat.*, pp. 18–19, 2011, [Online]. Available: http://gen-lab.hu/dokumentumok/solv_misc.pdf.

[35]   D. I. Svergun, "Restoring low resolution structure of biological macromolecules from solution scattering using simulated annealing," *Biophys. J.*, vol. 76, no. 6, pp. 2879–2886, 1999.

[36]   M. Burian, G. Fritz-popovski, and M. He, "Considerations on the model free shape retrieval of inorganic nanocrystals from SAXS data," pp. 1–6.

[37]   J. Ahrens, B. Geveci, and C. Law, *ParaView: An End-User Tool for Large Data Visualization*. 2005.

[38]   B. W. Goodfellow, Y. Yu, C. A. Bosoy, D. Smilgies, and B. A. Korgel, "The Role of Ligand Packing Frustration in Body-Centered Cubic (bcc) Superlattices of Colloidal Nanocrystals," 2015.

[39] K. Bian, J. J. Choi, A. Kaushik, P. Clancy, D. M. Smilgies, and T. Hanrath, "Shape-anisotropy driven symmetry transformations in nanocrystal superlattice polymorphs," *ACS Nano*, vol. 5, no. 4, pp. 2815–2823, 2011.

[40] D. V Talapin, E. V Shevchenko, and C. B. Murray, "Dipole-Dipole Interactions in Nanoparticle Superlattices," pp. 1–7, 2007.

[41] E. V. Shevchenko, D. V. Talapin, N. A. Kotov, S. O'Brien, and C. B. Murray, "Structural diversity in binary nanoparticle superlattices," *Nature*, vol. 439, no. 7072, pp. 55–59, 2006.

[42] B. W. Goodfellow, R. N. Patel, M. G. Panthani, D. M. Smilgies, and B. A. Korgel, "Melting and sintering of a body-centered cubic superlattice of PbSe nanocrystals followed by small angle X-ray scattering," *J. Phys. Chem. C*, vol. 115, no. 14, pp. 6397–6404, 2011.

[43] I. Lokteva, M. Koof, M. Walther, G. Grübel, and F. Lehmkühler, "Monitoring Nanocrystal Self-Assembly in Real Time Using In Situ Small-Angle X-Ray Scattering," *Small*, vol. 15, no. 20, pp. 1–8, 2019.

[44] W. G. Burgers, "On the process of transition of the cubic-body-centered modification into the hexagonal-close-packed modification of zirconium," *Physica*, vol. 1, no. 7–12, pp. 561–586, 1934.

[45] O. M. Londoñ, P. Tancredi, P. Rivas, D. Muraca, Leandro M. Socolovsky, and M. Knobel, "Handbook of Materials Characterization," *Handb. Mater. Charact.*, no. September, pp. 1–613, 2018.

[46] J. Keckes, "X-ray Production : Characteristic Radiation," 2022.